Numerical Analysis of Atmospheric Perturbations Induced by Large Wildfire Events

Authors: J. M. Haw[1], A. Farguell[1], C. B. Clements[1], D. B. Sapsis[2], and A. K. Kochanski[1]

[1]Wildfire Interdisciplinary Research Center, San Jose State University.

[2]California Department of Forestry and Fire Protection

Corresponding author: Adam Kochanski (adam.kochanski@sjsu.edu)

Key Points:

- The plume-dominated fire was found to follow the diurnal cycle, while the wind-driven fire was much less variable.
- Local winds in the plume-dominated fire had a much greater impact than those in the wind-driven fire, which had stronger non-local winds.
- A plume-dominated fire may promote strong convection leading to more rainfall and decreased fire activity through increased fuel moisture.

Abstract

This study analyzes fire-induced winds from a wind-driven fire (Thomas Fire) and a plume-dominated fire (Creek Fire). Two numerical experiments, one without the fire present and the other with the fire, were used. The fire-induced perturbations were then estimated by subtracting a variable value in the "No Fire Run" from the "Fire Run" (Fire - No Fire). For this study, spatial and temporal variability of winds, geopotential height, and convergence were analyzed. Furthermore, cloud water mixing ratio, precipitation, and fuel moisture were analyzed during the Creek Fire to assess fire-induced rainfall and its impact on fuel moisture. It was found that the wind-driven Thomas Fire created more widespread and generally stronger fire-induced winds than the plume-dominated Creek Fire. In addition, fire-induced wind speeds during the Creek Fire followed a diurnal cycle, while the Thomas Fire showed much less temporal variability. When analyzing geopotential height, the results were very similar to other idealized simulations. A localized low-pressure region was observed in front of the fire front, with a preceding high-pressure area. When analyzing precipitation, it was found that the fire increased precipitation accumulation in the area surrounding the active fire. This created an increase in fuel moisture which could have helped locally decelerate the fire spread. Further research into the processes behind fire-atmosphere interactions will lead to a better understanding of fire behavior and the extent to which these interactions can impact the fire environment. These studies will help assess the limitations of uncoupled operational models and improve fire modeling overall.

Plain Language Statement

This study analyzes winds caused by fire from both the Thomas Fire and the Creek Fire. These fires were chosen because the Thomas Fire was driven by strong winds, while the Creek Fire generated a towering smoke plume which influenced its growth. In addition to wind speed, geopotential height at multiple levels was analyzed to understand how deep into the atmosphere the fire effects are visible. Furthermore, precipitation was analyzed for the Creek Fire to see if there was any effect on how moist the surface fuels around the fire were. It was found that the Thomas Fire created more widespread and generally stronger winds than the Creek Fire throughout the simulation duration. In addition, wind speeds during the Creek Fire followed a daily cycle of high and low speeds, while the Thomas Fire did not. Changes in geopotential height also were found in the upper atmosphere which shows the far-reaching effects of the fire.

When analyzing precipitation, we found that the fire increased precipitation amounts around the fire area. This increased the surface fuel moisture which likely helped slow the fire spread.

1 Introduction

Fires are known to enhance the winds in the vicinity of the fire front, which in turn drive fire propagation and impact overall fire behavior (Sun et al., 2009). To help understand this phenomenon, a number of previous studies have analyzed fire-wind enhancement. One of the first such studies was the field experiment conducted by Quintiere, (1989), in which a prescribed burn was carried out in forest debris in an extensively instrumented area. The results from this study found that fire-induced winds reached up to 12 m/s and indicated the possibility of fire-induced cloud formation as well as possible lightning. Filippi et al., (2009) then used the MesoNH-ForeFire, a mesoscale model coupled with a tracer-based fire model, in the first study to use a coupled simulation to estimate how much a wildfire's convection can alter surrounding atmospheric conditions. Based on the idealized simulations of three fires, they found that in the case of a fire with large line ignition, the acceleration of winds towards the plume base increased an order of magnitude compared to the ambient wind speed. They also found that the simulated fire-induced winds from the study matched with similar values from large-scale wildfire studies using standard plume theory (Filippi et al., 2009). This study was mainly conducted on relatively small-scale fires under conditions similar to that of a prescribed burn. Later, Eftekharian et al., (2019) used OpenFOAM, a computational fluid dynamics software, to model and investigate the effects of both a point ignition and a line ignition on a small, idealized fire simulated in a 34×9×15 m domain (X×Y×Z). They found that longitudinal flow was greatly enhanced for the line ignition, while vertical flow was further enhanced by the point ignition. In a further study, Eftekharian et al., (2021) found that the greatest wind enhancement was co-located with elevated flame temperatures and occurred near the center lines of fire-induced vorticities.

Although many studies have indicated the importance of fire-induced winds in shaping the near-fire environment, none have quantified these effects in a case of a large wildfire. Also, the small scale of the numerical experiments conducted up to date precluded any analysis of the large-scale impacts of pyroconvection. For example, the vertical extent of the fire-induced perturbations, the impact on geopotential height, cloud development, precipitation, and resulting fuel moisture have not been studied in wildfire scenarios. In addition, none of the studies so far attempted to quantify both the temporal variability and the spatial extent of the fire-induced perturbations. Up to now, no numerical study has been conducted on the dynamical feedback loop involving fire-induced precipitation and its impact on fuel moisture and fire behavior. The only similar studies used reanalysis datasets to understand fire-induced rainfall suppression mechanisms for convective rainfall in sub-Saharan Africa (Saha et al., 2017).

In the context of fire-atmosphere coupling, wildfires are often classified as wind-driven, or plume-dominated (Byram, 1959). It is generally assumed that in case of the wind-driven fires, the power of the wind dominates the buoyancy and the fire itself does not impact local weather conditions. The plume-dominated fires, on the other hand, are generally associated with the conditions when the fire-induced buoyancy significantly impacts local winds controlling fire behavior (Sullivan, 2007). The distinction between these two regimes can be determined by calculating the Clark Convective Froude Number (F_c) or Byram's Convective Number (N_c), see Morvan & Frangieh, (2018). If $F_c^2 > 1$, then the fire can be classified as wind-driven, and the near-fire flow does not significantly respond to the fire-induced buoyancy. If $F_c^2 < 1$, the fire can be classified as plume-dominated, as the flow responds strongly to the fire-induced heating and convection (Sullivan, 2007). If Byram's Convective Number is used, the critical value of 10 can be used as a threshold. In this case, if $N_c > 10$ the fire is wind-driven, and if $N_c < 2$, the fire is plume-dominated (Morvan & Frangieh, 2018). For the purposes of this study, N_c was analyzed to confirm the fire regime.

The overarching goal of this study is to advance our understanding of the role of fire-atmosphere coupling processes in shaping the fire environment during large wildfires. To achieve this goal, the presented study investigates fire-atmosphere interactions, as well as quantifies the spatial and temporal effects of fire-induced perturbations in winds, geopotential height, precipitation, and fuel moisture, in two wildfires representing the wind-driven and plume-dominated regimes (Thomas Fire and Creek Fire, respectively).

2 Methods

$$N_c = \frac{2gI}{\rho c_p \theta_a (u - ROS)^3} \qquad \text{Equation 1}$$

To verify that the selected wildfires represent both the wind-driven and plume-dominated regime, an N_c analysis was performed. N_c was determined by Equation 1, in which g is the gravitational constant (9.8 m/s^2), I is the fireline intensity (kW/m), ρ is air density (1.2 kg m^{-3}), c_p is the specific heat of dry air (1.005 J kg^{-1} K^{-1}), θ_a is the absolute ambient air temperature (K), *u* is the mean wind speed (m/s), and *ROS* is the rate of spread of the fire (m/s). The average N_c value over the studied period was 29.34 for the Thomas Fire (4 December 2017 18Z – 8 December 2017 00Z) and 7.35 for the Creek Fire (5 September 2020 00Z – 15 September 2020 00Z). This confirmed the wind-driven character of the Thomas Fire, and the mixed character of the Creek Fire which transitioned from the wind-driven regime on the day of ignition, to the plume-dominated regime for the remainder of the studied period.

In order to analyze the fire-induced perturbations, first, historical fire progressions were reconstructed based on satellite observations and infrared perimeters. Fire detections from VIIRS and MODIS satellites along with the airborne infrared fire perimeters were used to reconstruct fire progression history using the Support Vector Machines (SVM) method proposed by Farguell et al., (2021). This method leverages the SVM to find a 3D surface defining the boundary between burnt and unburnt regions in the latitude/longitude/time space. Since the cross-sections of this surface at an arbitrary time represent fire extent, this method provides fire arrival maps by time step that enable reconstruction of fire spread over time.

In order to analyze the fire-induced perturbations, two different WRF-SFIRE runs were conducted, one with the fire present, and the other purely meteorological. WRF-SFIRE is a coupled fire-atmosphere model with a weather forecasting model coupled to a fire spread model (Mandel et al., 2011). These are called the Fire run and No Fire run, respectively. Both runs also utilized a fuel moisture model, containing 1, 10, and 100 hour moisture classes, to trace the fire impact on fuel characteristics. Subtracting these two runs (Fire - No Fire) allowed us to analyze the fire impacts on a given variable similarly as it was done to estimate the extents of fire effects in Kochanski et al., 2018. In the fire simulations, the fire progression was constrained using the fire histories derived using the SVM method mentioned above, in order to reduce the potential impacts of the inaccuracies in the fire spread representation. This approach mimics the widely used approach in meteorology where the reanalysis data is used to force the atmospheric model, but here the fire progression is used to force the fire spread model. The comparison between the Fire and No Fire runs enabled a detailed analysis of a wide range of fire-induced perturbations. For the purposes of this study, wind speed, geopotential height, and convergence were analyzed, along with cloud water mixing ratio, accumulated precipitation, and fuel moisture. Wind speed was studied in order to determine the temporal and spatial variability in fire-induced winds. Vertical cross-sections of winds and temperature were also studied to analyze the vertical extent of fire-induced circulations. Additionally, geopotential height was examined to determine the vertical extent of the fire-induced pressure perturbation. Then, wind convergence was explored to provide reasoning for fire-induced behavior and spread. Finally, the cloud water mixing ratio, rain, and fuel moisture were investigated in order to investigate the fire-atmosphere coupling, including the impact of precipitation on fuel moisture.

To be able to analyze this coupling mechanism, a radar analysis was performed to assess whether days in which there were clouds ended up producing rainfall. Specifically, the Differential Reflectivity and Correlation Coefficient were utilized to isolate rain from other features present in the radar image. An elevation angle of 1.82° was used to eliminate most of the noise seen in the lower levels of the atmosphere and focus more on the mountainous regions. Differential Reflectivity and Correlation Coefficient were used to distinguish between rain and smoke (smoke has generally higher differential reflectivity and lower correlation coefficient than rain (Melnikov et al., 2009; Jones et al., 2009; Zrnic et al., 2020; Aydell & Clements, 2021).

2.1 Numerical Analysis of Fire-Induced Perturbations

2.1.1 Wind-Driven Fire

The Thomas Fire began in Ventura County on 4 December 2017 during the longest period of Santa Ana Wind conditions recorded over the past 70 years (Fovell & Gallagher, 2018). These winds fanned two independent ignitions into a giant conflagration which ultimately became the largest wildfire for that time in modern California history. Winds near the areas of ignition were gusting up to 35 m/s and quickly fanned the fires rapidly toward the ocean (Fovell & Gallagher, 2018). By the time the fire was fully contained on 12 January 2018, the fire had scorched 281,893 acres, destroyed 1060 structures, and burned through both Ventura and Santa Barbara Counties (CAL FIRE, n.d.).

The Thomas Fire was modeled using two nested domains (1.33 km and 444 m resolution), as shown in Figure 1, for three days and six hours. The simulation covered the period from 4 December 2017 18Z until 8 December 2017 00Z. Table 1 shows the model configuration used for this simulation. The boundary and initial conditions were derived from the 3km High-Resolution Rapid Refresh (HRRR) product (Benjamin et al., 2016), using the WRFx forecasting system (Mandel et al., 2019).

Table 1

Configuration of the Thomas Fire simulation

Domains	**d01**	**d02**
Dimensions	118 x 82 x 41	211 x 118 x 41
Fire Mesh	N/A	2110 x 1180
Horizontal Grid Spacing (Atmosphere)	1333 m	444 m
Horizontal Grid Spacing (Fire)	N/A	44 m
Time Step	3 s	1 s
Microphysics	Thompson ARW NMM Option 8	Thompson ARW NMM Option 8
PBL Physics	ACM2 Option 7	ACM2 Option 7
Surface Model	ACM2 Option 7	ACM2 Option 7
Cumulus Parameterization	Kain-Fritsch Option 1	Kain-Fritsch Option 1
Radiation	RRTMG Option 4	RRTMG Option 4
Meteorological Forcing	HRRR	d01

2.1.2 Plume-Dominated Fire

The Creek Fire began in Fresno County on 4 September 2020, between the San Joaquin River and Shaver Lake (CAL FIRE, n.d.). Right after ignition, it was driven by powerful winds up the San Joaquin drainage, which caused it to explode in size and create a massive pyroCb cloud which continued to affect fire behavior (Jenner, 2020). Due to the effect of the massive plume, the Creek Fire was later able to spread quickly, despite weak diurnal winds in the fire region. It managed to become the largest wildfire in modern California history by 2020 standards after burning 379,895 acres in both Fresno and Madera Counties. The fire also destroyed 856 structures, damaged 71 structures, and caused 26 injuries. It was fully contained on 24 December 2020 (CAL FIRE, n.d.).

The Creek Fire was modeled using three nested domains (Figure 2). Table 2 shows the domain configuration used for this simulation. The simulation was conducted from 5 September

2020 00Z until 15 September 2020 00Z, for a period of 10 days. The resolution of the outer domain (d01) was 5000m, the intermediate domain (d02) was 1666 m, and the fire domain (d03) was 555 m. The boundary and initial conditions were generated from the Climate Forecast System Reanalysis (CFSR) data (Saha et al., 2010).

Table 2

Configuration of the Creek Fire simulation.

Domains	**d01**	**d02**	**d03**
Dimensions	196 x 196 x 41	196 x 196 x 41	196 x 196 x 41
Fire Mesh	N/A	N/A	3920 x 3920
Horizontal Grid Spacing (Atmosphere)	5000 m	1666 m	555 m
Horizontal Grid Spacing (Fire)	N/A	N/A	27 m
Time Step	30 s	7 s	2 s
Microphysics	Thompson ARW NMM Option 8	Thompson ARW NMM Option 8	Thompson ARW NMM Option 8
PBL Physics	MYNN2 Option 5	MYNN2 Option 5	MYNN2 Option 5
Surface Model	GFS Option 3	GFS Option 3	GFS Option 3
Cumulus Parameterization	Kain-Fritsch Option 1	0	0
Radiation	RRTMG Option 4	RRTMG Option 4	RRTMG Option 4
Meteorological Forcing	CFSR	d01	d02

3 Results

3.1 Wind-Driven Fire

The Thomas Fire was primarily wind-driven and fanned by strong, gusty winds and burned in mountainous terrain. For this fire event, wind speed and geopotential height were analyzed to see how these factors were influenced over and in the vicinity of the fire. First, the spatial variability of 10 m winds was analyzed, then we investigated the vertical wind speed cross sections along two lines parallel and perpendicular to the main fire direction, and finally, the temporal variability in the wind perturbation was investigated.

3.1.1 Analysis of Surface Fire Winds During a Wind-Driven Fire

The fire-induced wind speed perturbation analyzed here is the difference between the wind speed from the Fire and No Fire Runs and will be referred to in the text as fire-induced wind or fire wind. According to Figure 3, intense fire winds occurred around the start of the fire on 5 December, with values exceeding 10 m/s downwind of the fire front. The areas of fire-induced winds occurred directly downstream from the areas of active fire, which indicates that these areas occurred within or surrounding the smoke plume as it was advected by the strong Santa Ana Winds. It was also noticed that areas of strong positive fire-induced winds were usually surrounded by weaker negative fire-induced winds, which could be associated with the inflow zones to that region of the fire. The fire rate of spread in deceleration regions (blue) was significantly slower compared to acceleration regions highlighted in red.

While Figure 3 shows the maximum surface fire winds over the entire domain of the fire from a horizontal vantage point, Figure 4 provides vertical cross-sections through the fire in order to investigate the vertical structure of fire winds. Figure 3 demonstrates the locations of these cross-sections. The cross-section in Figure 4a was chosen as it follows the wind direction of the Santa Ana Winds, as well as the rapid initial expansion of the fire. It shows that the strongest fire-induced wind speeds align with the time when the fire passes through cross-section a) as seen in Figure 3, thus demonstrating that the wind perturbation is associated with the fire activity. In addition, the isotherms indicate the mountain wave pattern, which is very apparent over the higher mountains, as well as several hydraulic jumps (not pictured) at later time steps. When looking at the areas of strong fire-induced winds, there are areas of much stronger winds around the surface, and much weaker winds just above the surface. These two lobes are separated by an isotherm, which demonstrates that the presence of fire-induced winds shown in Figure 4a disrupts the mountain wave pattern. These factors all suggest that the fire aids in altering the vertical thermal gradient by pushing isotherms upward in the atmosphere near the fire front. This helps alter wind speeds and patterns over the mountain range by disrupting the mountain wave and transferring upper-level momentum to the surface and leads to an increase in the surface winds at the expense of the winds aloft.

The vertical cross-section b), shown in Figure 4b, was chosen to demonstrate the fire-induced winds across the main fire propagation direction. This cross-section, perpendicular to the predominant wind direction, was studied to verify if the mountain wave perturbation also occurs across the fire. Unlike the streamwise cross-section presented in Figure 4a, the region of accelerated surface winds is much wider here but is still associated with the upper-level wind speed decrease. This indicates an energy transport from higher elevations to the surface in response to the fire-induced buoyancy, which extends across the fire area. Unlike the streamwise cross-section, the look at the wind structure perpendicular to the wind indicates the secondary lobe of strong fire-induced winds, which occurred away from the fire front. This remote acceleration zone, located right from the peak of the fire heat flux in Figure 4b, corresponds to the region of accelerated winds evident in the northwest direction from the fire front in Figure 3a.

3.1.2 Temporal Variability of Fire Winds

The time series of maximum magnitude of surface (10 m) fire winds is shown in Figure 5. This figure highlights that the period of strongest fire-induced winds (up to 15 m/s) occurred during the initial expansion of the fire when it was getting fanned by strong Santa Ana Winds. After this initial period (ending 12-05 18z), the fire winds decreased, but remained generally in the 4 – 8 m/s range, with few isolated spikes exceeding 9 m/s. There was no diurnal cycle present either in the winds or the fire activity because of consistent high fire intensity in response to low relative humidity and persistent Santa Ana Winds present throughout that period.

3.1.3 Statistics of local and non-local fire-induced wind perturbations

The boxplots are a good way to visualize how the range of the surface fire winds changes from day to day on both non-local and local scales. In this case, non-local refers to the fire winds over the entire domain (as in Figure 5), and local refers to fire winds surrounding areas of active fire or areas already burned. Figure 6a shows that on a daily basis, the average non-local fire winds vary significantly, with an average speed ranging up to 7 m/s on 5 December. There are also several outliers with fire-induced speeds up to 12 m/s on 7 December.

In terms of local fire winds around the burned areas (Figure S1), fire-induced winds averaged around near zero, but there were many outliers here as well, with fire-induced speeds as low as -0.5 m/s, and ranging up to 1.9 m/s. The same overall pattern was seen around areas of active fire (Figure 6b) but with more extreme speed outliers, particularly on 6 December and 7 December. Of note is that on 7 December, there were outliers indicating -1.0 m/s and 0.9 m/s. These observations demonstrate that most of the stronger fire-induced winds are advected downstream of the main fire front and are non-local. Thus, local fire-induced winds tend to be much weaker, with occasional stronger gusts, as indicated by the outlier values.

3.1.4 Geopotential Height Analysis

In order to analyze the fire's influence on the atmospheric conditions around it, geopotential height perturbations were analyzed at three different levels: surface, 600mb, and 500mb. These levels have been selected to investigate the spatial pattern of the pressure perturbation associated with the surface winds directly interacting with the fire, as well as the vertical extent of the fire-induced wind perturbations. Geopotential height was analyzed due to its relationship with temperature and the density of air. It is also particularly useful to analyze trends associated with surface pressure in the upper atmosphere, as it can inform about how much the height of a pressure level has changed due to the presence of fire. The fire-induced surface geopotential height perturbation, as well as the wind vector field for both the Fire (red) and No Fire (blue) runs, are shown in Figure 7. The surface level (745 hPa) was chosen as the level just above the highest elevation of the terrain within the domain. The wind field indicates the characteristic Northeast direction of the Santa Ana Winds pushing the fire very quickly to the Southwest during the initial rapid expansion to the coast on 5 December. During this time, there were relatively intense geopotential height perturbations of up to 5.20 m and -3.10 m. These perturbations occurred directly downstream from where the fire was burning and tended to drift off downwind, advected by the ambient winds. This occurred due to the buoyancy of the smoke plume, as the smoke was carried into the upper atmosphere, and the air density decreased. At the same time, the Santa Ana Winds pushed the plume downstream, resulting in a tilt and increased perturbations, as well as increased fire-induced winds downwind from the firefront. Faster fire rate of spread (associated with higher intensity) tended to produce stronger geopotential height perturbations, and these perturbations influenced the direction and strength of the wind field as they were carried off with the smoke plume. In some cases, the perturbations helped steer the fire to the West and push it downwind. In addition, areas of lower geopotential height tended to occur right in front of the firefront, with areas of higher geopotential height preceding the lower geopotential height.

The time series of geopotential perturbations directly around the fire were analyzed in order to quantify the local impact of the fire on the surrounding atmosphere and to analyze its time evolution. The perturbations were calculated by subtracting the values of the No Fire run from the values of the Fire run (Fire – No Fire). The maximum difference from each time step was then plotted. This enabled the analysis of how changes in the fire activity alter the geopotential height over time. The analysis was done first by looking at the geopotential height within the entire burned area, but these differences (not shown) came out to be minor, indicating that most significant perturbations were associated with regions of the active fire front itself not within the whole fire perimeter. This is more easily observed by looking at Figure 8, which shows the perturbation time series for each level analyzed around areas of actively burning fire. When the fire first started rapidly expanding on 5 December, the perturbations were mainly positive, with differences up to 2.2 meters for the surface level (Figure 8a). As the fire started to grow larger, the perturbations increased, with perturbations of up to 4.7 m. After this point, the perturbations decreased, with occasional intense spikes on each day, with the most intense ones occurring on 7 December, with a value of 5.2 m. Each set of the spikes, particularly on 5 December, occurred at the same time as the spikes in fire-induced winds shown in Figure 5, demonstrating the linkage between fire winds and surface geopotential height perturbations.

The patterns in the two upper levels of the atmosphere were similar as well, except with much smaller variation in perturbations. In Figure 8c, at the 500 hPa level, perturbation variation increased up to 2.3 meters, which demonstrates that the effects of the fire extend into the upper atmosphere. This spike also matched with the peak in fire-induced wind speeds on 5 December, likely indicating the development of pyrocumulus clouds which reached the upper levels of the atmosphere during this time. Minimal variability occurred after 5 December at the 600 hPa layer (Figure 8b), indicating that the strongest perturbations were occurring downwind from the fire itself. However, at the 500 hPa layer (Figure 8c), small spikes occurred intermittently throughout the day. These spikes occurred at the same time as those from the 600 hPa layer (Figure 8b) but with slightly lower magnitudes on 5 December and slightly higher magnitudes at later times. This suggests that fire-induced perturbations expand vertically as more smoke reaches the upper levels of the atmosphere at later times during the Thomas Fire.

When analyzing the minimum perturbations for each level (Figure S2), patterns were seen to be similar, but negative, indicating the presence of both positive and negative perturbations along the firefront. The only exception to this pattern was at the 500 hPa level where a major spike of -4.8 meters occurred on 5 December. This aligns with the major spike in the maximum perturbation as well, which could suggest the presence of strong updrafts and downdrafts in the upper levels, which could create erratic fire behavior at the surface.

3.1.5 Spatial Analysis of Wind Convergence

To complement the fire wind speed and geopotential analysis, we also analyzed wind convergence, a phenomenon in which winds are pulled toward a given area, usually an area of low pressure. As seen in Figure 9, convergence occurs mainly in front of the fire front, with divergence preceding the convergence zone. The zoomed-in image of Figure 9 shows the streamlines converging ahead of the fire front, which produced the convergence zone, or area of low pressure, there. This behavior does not occur with the No Fire run (see the blue vectors in Figure 7), which indicates the local flow modification due to the fire. This is consistent with the findings of Clark et al., (1996), indicating a convective column forming above a low-pressure center in front of the fire front which alters local wind speed and direction.

3.2 Plume-Dominated Fire

The Creek Fire is an important fire to analyze as it was mainly plume-dominated. This means that there were overall weak winds, and the fire was primarily driven by conditions induced, or enhanced by, the pyroconvective column above it, or by other forces such as terrain and fuels. The Creek Fire started amidst some gusty up-canyon winds during its initial explosive expansion, but after the first day, it continued to expand at rapid rates without the presence of strong atmospheric forcing. For the Creek Fire, the variables of wind speed (Figure 10 – Figure 12), geopotential height (Figure 13 – Figure 14), and convergence (Figure 15) were analyzed. Due to significant pyroactivity, water vapor mixing ratio (not shown), precipitation (Figure 17), and fuel moisture (Figure 18) were also examined. Spatial variability of wind speed and geopotential height were first investigated, followed by a temporal analysis. The rest of the variables were analyzed in the context of spatial patterns.

3.2.1 Analysis of Surface Fire Winds During a Plume-Dominated Fire

After the initial explosion of the fire on 5 September, when the fire-induced winds were both strong and widespread, the character of fire-induced wind perturbation changed. They became more localized and consistent with the diurnal pattern corresponding to large periods of growth during the day and reduced activity at night. Figure 10a shows the initial explosive growth of the fire. After this point, there was a lot of fire growth under conditions very similar to the No Fire run (no significant fire-induced winds), except for localized areas of stronger winds outside of the fire perimeter. As seen in Figure 10a, an area of weaker fire-induced winds (inflow zone) appears ahead of the fire front and is accompanied by large areas of much stronger fire-induced winds. This same pattern occurs throughout the period studied, with areas of inflow almost always accompanying times of high fire-induced winds. This behavior is consistent with findings from idealized simulations by Clark et al., (1996), indicating a low-pressure area ahead of the fire front drawing winds in from all directions. This leads to enhanced winds along the fire front and decreased winds throughout the inflow zone. However, after the Creek Fire's initial wind-driven expansion, areas of fire-induced winds became very localized and did not extend downwind, as seen in Figure 10b. This indicates a significant change in the character of the fire winds from remote mostly downwind from the fire to more local associated directly with the fire activity.

3.2.2 Temporal Variability of Fire Winds During a Plume-Dominated Fire

The most notable aspect of the time evolution of the fire-induced winds presented in Figure 11 is the consistent diurnal pattern. This is unlike the Thomas Fire, which initially experienced very strong fire winds, which decreased significantly after the first day. The Creek Fire, for the most part (except on 12 September), saw fire-induced winds following the diel trend. On each day, wind speeds peaked at approximately 1:00 AM local time (08:00 UTC) and saw a sharp decrease at around 7:00 PM local time (02:00 UTC). This shows that the fire-induced winds peak during the early morning hours and last throughout the day, and subsequently decrease during the evening and late-night hours. This can be because winds in the early morning are generally very calm, but with the presence of the fire creating its own wind, there is a much larger difference between Fire and No Fire wind speeds. On 12 September, the whole day experiences relatively calm fire-induced winds, which can be attributed to increased cloud cover and rainfall associated with fire-induced precipitation. With reduced solar heating and convective activity, the winds became calmer.

3.2.3 Statistics of local and non-local fire-induced wind perturbations During a Plume-Dominated Fire

The boxplots shown in Figure 12 help to visualize the Creek Fire's non-local and local fire-induced wind speeds over each day. Figure 12a shows that over the whole domain, the average maximum wind speed is consistent at around 7 m/s on each day. This is different than during the wind-driven fire which experienced more day-to-day variability. The greatest variability occurred on 12 September, when fire winds ranged from 11.5 m/s to 0.8 m/s. The days with the least range between the first and fourth quartiles are 5 September and 6 September, which were the days with a major wind event that caused the initial blow-up of the fire. Unlike during the wind-driven Thomas Fire, here no outlier wind speeds were observed. This is significant because it indicates that in the plume-dominated fire, the fire winds were less random and more closely related to the fire activity, thus supporting the notion that plume-dominated fires can create their own local weather conditions.

Figure 12b investigates the winds only over areas of active fire progression (where fire-released heat flux is positive). For each day, the average maximum fire-induced wind speed is slightly positive at around 0.2 m/s. It indicates that the fire generally accelerates winds near the fire front. Additionally, each day has lots of positive fire-induced wind outliers, indicating regions of strong fire-induced winds. The analysis of the local and non-local fire effects during the plume-dominated regime reveals that it has a unique character when compared to the wind-driven fire. Here, the non-local effects are weaker than during the wind-driven fire, however, the local fire effects are much stronger (up to 9 m/s compared to 0.75 m/s). The strong local fire effects show that the plume-dominated fire creates stronger near-fire winds than the wind-driven fire. This effect means that despite the weaker remote fire winds compared to the wind-driven case, strong local fire-induced winds in a plume-dominated fire can be a much more significant driving force of fire spread than during a wind-driven fire.

3.3 Geopotential Height Analysis During a Plume-Dominated Fire

According to the conducted analysis, the geopotential height perturbations for the Creek Fire were the strongest and most widespread at the surface level (629 hPa). Other perturbations, particularly those seen in Figure 13, could be due to outside forces such as thunderstorms. In addition, all figures demonstrate that the strongest perturbations around the fire perimeter were associated with increased fire activity. During these times, the surface perturbations were generally over 0.7 m. When the fire became more plume-dominated, the geopotential height perturbations became much smaller and much more localized. Perturbations stretched out from the fire in the direction of the predominant wind. Therefore, it can be deduced that these perturbations were associated with the advection of the positively buoyant plume. Similar to the Thomas Fire, the perturbations for the Creek Fire also caused a change in wind speed and direction as they propagated away from the fire.

Aside from the spatial variability, the time evolution of the geopotential perturbation at various heights was investigated as well. The analysis of the time series presented in Figure 14 reveals many interesting phenomena that occurred with these perturbations over the active fire. The same analysis was performed for minimum perturbations (figure not shown), and many of the same patterns were found for each level. At the surface level (Figure 14a), a spike was noted on 9 September with a perturbation of 48 m at the surface (spike extending beyond the plot) and 4.8 m at 600 hPa (Figure 14b). This spike did not reach the upper atmosphere in any large way, which suggests potentially intense fire behavior at the surface. Some similar spikes of up to 6.5 m on 6 September and 7 September also occurred. The same spikes were noticed at both the 600 hPa and 500 hPa levels as well. At the 600 hPa level (Figure 14b), these spikes were very similar at around 4.9 and 7.0 m, respectively. Similar perturbations occurred at the 500 hPa level (Figure 14c), but to a much greater extent, around 17.7 meters. These major perturbations signify the presence of pyrocumulonimbus clouds hitting the upper levels of the atmosphere over the fire area. Mostly small perturbations occurred throughout the remaining period studied, alluding to the plume-dominated nature of this event. Since much larger perturbations were seen outside of the fire perimeter in Figure 13, a detailed analysis was carried out to determine whether these outside perturbations were due to rain-causing thunderstorms or other factors.

3.4 Spatial Analysis of Convergence

Many of the similar findings are present when analyzing the wind convergence field during the Thomas and Creek Fires. The streamlines still converge ahead of the firefront, creating a convergence zone in Figure 15. However, here, it is clearer that convergence tends to occur in valleys, while divergence occurs along ridges and mountain tops. This could be another explanation as to how the Creek Fire spread so fast despite the lack of strong winds present. Naturally forming convergence zones likely played a large part in the fire's spread as well.

3.5 Analysis of Fire Effects on Cloud Activity and Precipitation

Since the Creek Fire was associated with significant cloud activity, here we investigate fire-induced impacts on cloud formation. The goal is to determine whether the geopotential height perturbations over and nearby the Creek Fire were associated with thunderstorms/cloud development. Additionally, we investigate if the fire-induced cloud activity resulted in precipitation that could increase the fuel moisture.

The first step in determining whether geopotential perturbations were associated with thunderstorms was to see if any clouds were simulated over the area. To do this, the cloud water mixing ratio was examined. Over the full ten days of the simulation, clouds formed on September 5, 6, 7, 8, and 11. To validate if these results were realistic, and if any precipitation was present, historical radar data was analyzed (see Figure 16).

When analyzing Reflectivity, there are many areas of energy present, with blue representing light disturbances and green/yellow representing heavier disturbances. However, it is necessary to determine which of these disturbances are actually rain and which are due to other factors, such as the smoke plume. When looking at Correlation Coefficient, areas of rain can be seen in areas of yellow to red (0.8 – 1). In Figure 16b, an area of rain puts a dent in the eastern flank of the fire and seems to slow down its eastward progression. Figure 16a also shows the Reflectivity plot at the same time to indicate the importance of using polarimetric radar variables to distinguish between the smoke plume, clouds, and rain (Ansari et al., 2008).

The estimates of rainfall from the radar analysis were then compared to the precipitation from the WRF-SFIRE model and the observations match up very well. Over the entire period studied, there was ~10 mm of precipitation from the Fire run, as seen in Figure 17a. To better understand how much of this precipitation was caused by the fire itself, fire-induced precipitation was quantified. As presented in Figure 17b, ~4.2 mm of the total precipitation can be attributed to the presence of the fire. This shows that during plume-dominated fires, aside from the positive fire feedback through the fire winds, there may be negative feedback where fire promotes stronger convection and cloud formation that leads to increased precipitation which can potentially decrease fire activity by increasing the fuel moisture.

In order to determine how much of an impact the rainfall had on the surrounding fuels, the overall dead fuel moisture was plotted in Figure 18. As seen there, these fuels change a lot, especially in places where it has rained. When comparing fuel moisture values in Figure 18 to the precipitation regions in Figure 17, it is apparent that fuel moisture values are between 21-27% in areas where it rained, and between 5-17% elsewhere. To determine how this impacted the fire itself, the potential rate of spread values over these regions from the Fire and No Fire runs were investigated. Values presented in Table 3, indicate that this rainfall, and the subsequent increase in fuel moisture, had the potential to slow down the spread of the fire by about 10% in regions affected by precipitation. These values for the rate of spread analysis were calculated by looking at the variable for fire rate of spread (ROS) within WRF-SFIRE, choosing the days in which it rained the most along the fire perimeter, and then choosing the spots along the fire perimeter which received the most rainfall.

Table 3

The rate of Spread comparison between the Fire and No Fire runs on two dates that had the most rainfall.

Date: 11 September 2020		Date: 12 September 2020	
Fire ROS	0.1725 m/s	Fire ROS	0.2476 m/s
No Fire ROS	0.195 m/s	No Fire ROS	0.2661 m/s
Percent Difference	13.04%	Percent Difference	7.47%

4 Summary and Conclusions

The purpose of this study was to analyze large-scale changes to surrounding atmospheric variables due to large wildfires in order to quantify the effect that a wildfire has on the conditions surrounding it. This is especially important for improving wildfire modeling, as well as providing better situational awareness to firefighters involved in fire suppression. Two different types of wildfires were analyzed, a wind-driven fire (Thomas Fire) and a plume-dominated fire (Creek Fire).

It was found that during the Thomas Fire, which was fanned by strong Santa Ana Winds, winds were up to 15 m/s faster in the simulation domain than they would have been if no fire were present. These maximum fire-induced winds also occurred when the prevailing Santa Ana Winds were strongest and most steady. Due to the presence of these strong winds, there was no diurnal cycle present. The fire-induced winds had a non-local character and extended up to 15-20 km downwind from the active fire. This could be particularly important in the context of fires exhibiting significant spotting. The fire embers landing in the regions of strong fire winds could result in spot fires propagating much faster than expected based on the ambient wind conditions.

During the plume-dominated Creek Fire, fire-induced winds experienced strong diurnal fluctuations and generally peaked in the early morning hours (around 08:00 UTC) and lasted throughout the day (around 02:00 UTC). Also unlike in the wind-driven case, here the fire winds were locally induced by the plume and the fire didn't cause widespread areas of strong wind acceleration as seen during the wind-driven Thomas Fire. Fire-induced winds were boosted by up to 12 m/s in localized areas. This is less than during the wind-driven Thomas Fire, however, the very local character of these winds could result in unexpected erratic fire behavior. The main differences between the two regimes are that wind-driven fires show little diurnal variability in the wind patterns and the strongest fire-induced winds occur downwind from the fire front, whereas plume-dominated fires follow a diurnal wind pattern and have very localized regions of fire-induced winds over the active fire regions.

In terms of geopotential height perturbations, it was found that in both fires, areas of positive and negative perturbations emanated out from the fire front following the primary wind direction and the buoyant column advected by the wind. For the Thomas Fire, these perturbations increased with atmospheric height, whereas they tended to decrease with height over the Creek Fire, except in very localized areas, which were found to be due to convective rain-producing clouds. Wind speed and direction around areas of perturbations were usually found to be drastically altered, which could have changed the fire behavior and spread to be more erratic. In addition, areas of lower geopotential height were found in front of the fire line, with higher geopotential heights preceding the lower height areas. This is consistent with the findings from Clark et al.,

(1996) on parabolic fire spread and convective columns, which produced an area of convergence ahead of the fire front, thus increasing the fire-induced winds.

Aside from highlighting the complexities in the character of the fire winds in wind-driven and plume-dominated fires, this study also affirmed that while fire can create winds that can quicken its spread and cause extreme fire behavior, it can also induce weather conditions reducing its activity. The analysis of fire-induced precipitation and its effect on the fuel moisture indicated that fire-induced precipitation could have helped slow fire growth by up to 13% in areas where it rained. This could have increased the effectiveness of fire suppression operations primarily on the eastern and northern flanks where the most rain occurred.

5 Limitations and Future Work

While these simulations provided a new way to analyze fire-induced circulations, much more work still needs to be conducted to fully understand these processes. For instance, these simulations were conducted with relatively low spatial resolution. For that reason, the estimates of the magnitude of fire-induced winds presented here are rather conservative. In reality, at small scales, these perturbations may be stronger. In addition, fuel load and fire intensity may have been underestimated due to instances of tree mortality and overall vegetation health that were not accounted for in this study. Having better knowledge and data on the vegetation in the modeled area would be needed to investigate and address these issues. Overall, conducting simulations in a higher spatial resolution could be beneficial to further understanding of these fire-induced circulations. However, it is important to note that the resolution used for the current study corresponds to the resolution used in operational fire forecasting with WRF-SFIRE and WRFx (Mandel et. al 2019). Therefore, this study shows to what degree fire-induced winds can be captured in coupled fire-atmosphere forecasts. In addition, extending the presented methodology to a larger number of fires, as well as direct measurements of the wind field near active wildfires, would help to further expand this study.

Acknowledgments

We would like to acknowledge high-performance computing support from Cheyenne (doi: 10.5065/D6RX99HX, provided by NCAR's Computational and Information Systems Laboratory, sponsored by the National Science Foundation). We are also grateful to the SJSU Fire HPC Support group for providing the computational assistance needed to carry out simulations model analyses shown here. This work was funded by CALFIRE grant 8GG21829*,* the SJSU Wildfire Interdisciplinary Research Center Grant 34-1505-0009, NSF grants IUCRC-2113931, and DEB-2039552 and NASA grants 80NSSC19K1091, 80NSSC22K1717.

Open Research

The WRF-SFIRE model used for the Fire and No Fire simulations in the study is available at GitHub via https://github.com/openwfm/WRF-SFIRE with public access (WRF-SFIRE, 2022). In addition, the data used for the radar analysis was found via NOAA's Weather Climate Toolkit, which can be downloaded for public use at https://www.ncdc.noaa.gov/wct/ (WCT, n.d.). The codes and data analysis used for this study can be found at https://github.com/wirc-sjsu/Fire-Induced-Circulations (wirc-sjsu, 2023).

References

Ansari, S., Hutchins, C., & Del Greco, S. (2008). *The NOAA Weather and Climate Toolkit*. *2008*, IN23B-1086.

Aydell, T. B., & Clements, C. B. (2021). Mobile Ka-Band Polarimetric Doppler Radar Observations of Wildfire Smoke Plumes. *Monthly Weather Review*, *149*(5), 1247–1264. https://doi.org/10.1175/MWR-D-20-0198.1

Baptiste Filippi, J., Bosseur, F., Mari, C., Lac, C., Le Moigne, P., Cuenot, B., Veynante, D., Cariolle, D., & Balbi, J.-H. (2009). Coupled Atmosphere-Wildland Fire Modelling. *Journal of Advances in Modeling Earth Systems*, *1*(4). https://doi.org/10.3894/JAMES.2009.1.11

Benjamin, S. G., Weygandt, S. S., Brown, J. M., Hu, M., Alexander, C. R., Smirnova, T. G., Olson, J. B., James, E. P., Dowell, D. C., Grell, G. A., Lin, H., Peckham, S. E., Smith, T. L., Moninger, W. R., Kenyon, J. S., & Manikin, G. S. (2016). A North American Hourly Assimilation and Model Forecast Cycle: The Rapid Refresh. *Monthly Weather Review*, *144*(4), 1669–1694. https://doi.org/10.1175/MWR-D-15-0242.1

Byram, G.M. 1959. Combustion of forest fuels. Pages 61–89 in: K.P. Davis, editor. Forest fire: control and use. McGraw Hill, New York, New York, USA.

Clark, T. L., Jenkins, M. A., Coen, J. L., & Packham, D. R. (1996). A Coupled Atmosphere-Fire Model: Role of the Convective Froude Number and Dynamic Fingering at the Fireline. *International Journal of Wildland Fire*, *6*(4), 177–190. https://doi.org/10.1071/wf9960177

Creek Fire | CAL FIRE. (n.d.). Retrieved January 26, 2023, from https://www.fire.ca.gov/incidents/2020/9/4/creek-fire/

Eftekharian, E., Ghodrat, M., He, Y., Ong, R. H., Kwok, K. C. S., & Zhao, M. (2019). Numerical Analysis of the Effect of Fire Source Configuration on Fire-Wind Enhancement. *Heat Transfer Engineering*, *42*(1), 41–60. https://doi.org/10.1080/01457632.2019.1685249

Eftekharian, E., Salehi, F., He, Y., & Kwok, K. C. S. (2021). LES analysis on the effects of baroclinic generation of vorticity on fire-wind enhancement. *International Journal of Thermal Sciences*, *162*, 106775. https://doi.org/10.1016/j.ijthermalsci.2020.106775

Farguell, A., Mandel, J., Haley, J., Mallia, D. V., Kochanski, A., & Hilburn, K. (2021). Machine Learning Estimation of Fire Arrival Time from Level-2 Active Fires Satellite Data. *Remote Sensing*, *13*(11), Article 11. https://doi.org/10.3390/rs13112203

Fovell, R. G., & Gallagher, A. (2018). Winds and Gusts during the Thomas Fire. *Fire*, *1*(3), Article 3. https://doi.org/10.3390/fire1030047

Jenner, L. (2020, September 8). *California's Creek Fire Creates Its Own Pyrocumulonimbus Cloud* [Text]. NASA. http://www.nasa.gov/feature/goddard/2020/californias-creek-fire-creates-its-own-pyrocumulonimbus-cloud

Jones, T. A., Christopher, S. A., & Petersen, W. (2009). Dual-Polarization Radar Characteristics of an Apartment Fire. *Journal of Atmospheric and Oceanic Technology*, *26*(10), 2257–2269. https://doi.org/10.1175/2009JTECHA1290.1

Kochanski, A. K., Fournier, A., & Mandel, J. (2018). Experimental Design of a Prescribed Burn Instrumentation. *Atmosphere*, *9*(8), Article 8. https://doi.org/10.3390/atmos9080296

Mandel, J., Beezley, J. D., & Kochanski, A. K. (2011). Coupled atmosphere-wildland fire modeling with WRF 3.3 and SFIRE 2011. *Geoscientific Model Development*, *4*(3), 591–610. https://doi.org/10.5194/gmd-4-591-2011

Melnikov, V. M., Zrnic, D. S., & Rabin, R. M. (2009). Polarimetric radar properties of smoke plumes: A model. *Journal of Geophysical Research: Atmospheres*, *114*(D21). https://doi.org/10.1029/2009JD012647

Morvan, D., Frangieh, N., Morvan, D., & Frangieh, N. (2018). Wildland fires behaviour: Wind effect versus Byram's convective number and consequences upon the regime of propagation. *International Journal of Wildland Fire*, *27*(9), 636–641. https://doi.org/10.1071/WF18014

NOAA's Weather and Climate Toolkit (Viewer and Data Exporter). (n.d.). Retrieved August 24, 2022, from https://www.ncdc.noaa.gov/wct/

Openwfm/WRF-SFIRE. (2023). [Fortran]. OpenWFM. https://github.com/openwfm/WRF-SFIRE (Original work published 2019)

Quintiere, J. G. (1993). Canadian Mass Fire Experiment, 1989. *Journal of Fire Protection Engineering*, *5*(2), 67–78. https://doi.org/10.1177/104239159300500203

Saha, M. V., D'Odorico, P., & Scanlon, T. M. (2017). Albedo changes after fire as an explanation of fire-induced rainfall suppression. *Geophysical Research Letters*, *44*(8), 3916–3923. https://doi.org/10.1002/2017GL073623

Saha, S., Moorthi, S., Pan, H.-L., Wu, X., Wang, J., Nadiga, S., Tripp, P., Kistler, R., Woollen, J., Behringer, D., Liu, H., Stokes, D., Grumbine, R., Gayno, G., Wang, J., Hou, Y.-T., Chuang, H., Juang, H.-M. H., Sela, J., … Goldberg, M. (2010). The NCEP Climate Forecast System Reanalysis. *Bulletin of the American Meteorological Society*, *91*(8), 1015–1058. https://doi.org/10.1175/2010BAMS3001.1

Sullivan, A. L. (2007). Convective Froude number and Byram's energy criterion of Australian experimental grassland fires. *Proceedings of the Combustion Institute*, *31*(2), 2557–2564. https://doi.org/10.1016/j.proci.2006.07.053

Sun, R., Krueger, S. K., Jenkins, M. A., Zulauf, M. A., Charney, J. J., Sun, R., Krueger, S. K., Jenkins, M. A., Zulauf, M. A., & Charney, J. J. (2009). The importance of fire–atmosphere coupling and boundary-layer turbulence to wildfire spread. *International Journal of Wildland Fire*, *18*(1), 50–60. https://doi.org/10.1071/WF07072

Thomas Fire | CAL FIRE. (n.d.). Retrieved January 16, 2023, from https://www.fire.ca.gov/incidents/2017/12/4/thomas-fire/

wirc-sjsu/Fire-Induced-Circulations. (n.d.). GitHub. Retrieved June 24, 2023, from https://github.com/wirc-sjsu/Fire-Induced-Circulations

Zrnic, D., Zhang, P., Melnikov, V., & Mirkovic, D. (2020). Of Fire and Smoke Plumes, Polarimetric Radar Characteristics. *Atmosphere*, *11*(4), Article 4. https://doi.org/10.3390/atmos11040363

Figure Captions

Figure 1: Setup of 2 domains for the Thomas Fire with fire ignition points shown.

Figure 2: Setup of 3 domains for the Creek Fire with fire ignition point shown.

Figure 3: Fire-induced 10 m wind speed over Domain 2 of the Thomas Fire on 5 December 2017 12:30:00 UTC. The black lines a) and b) correspond to the location of vertical cross sections shown in Figure 4a and Figure 4b.

Figure 4: Vertical cross section a) over the Thomas Fire showing fire-induced winds and temperature on 5 December 2017 12:30:00 UTC is shown on the left. Vertical cross section b) over the Thomas Fire showing fire-induced winds and temperature on 5 December 2017 12:15:00 UTC is shown on the right. The location of the fire front is denoted by the peaks in the Ground Heat Flux time series.

Figure 5: Maximum fire-induced wind speed in the Thomas Fire domain.

Figure 6: Boxplot a) shows the distribution of maximum fire-induced winds in the whole computational domain over each day. Boxplot b) shows the distribution of maximum fire-induced winds over each day around areas of active fire. The minimum and maximum values for the given day (excluding outliers) are represented by the lowest and highest lines, respectively. The box represents the 2nd and 3rd quartiles of the data, with the middle line representing the median of the data. Any outliers are represented by circles above or below the minimum and maximum value lines.

Figure 7: Fire-induced surface geopotential height perturbations and wind field over Domain 1 of the Thomas Fire on 5 December 2017 13:00:00 UTC. Blue arrows indicate wind vectors from the No Fire run and red arrows indicate wind vectors from the Fire Run.

Figure 8: Fire-induced surface geopotential height perturbations for the a) surface, b) 600 hPa, and c) 500 hPa pressure levels, over the regions of positive fire heat flux.

Figure 9: 10-meter Horizontal Convergence around the Thomas Fire as seen on 5 December 2017 12:30:00 UTC.

Figure 10: a) Fire-induced wind speeds over Domain 3 of the Creek Fire on 5 September 2020 23:00:00 UTC and b) fire-induced wind speeds over Domain 3 of the Creek Fire on September 6 23:30:00 UTC.

Figure 11: Maximum fire-induced wind speed over Domain 3 of the Creek Fire.

Figure 12: Boxplot a) shows the distribution of maximum fire-induced winds in the whole domain over each day. Boxplot b) shows the distribution of maximum fire-induced winds over each day around areas of active fire. The minimum and maximum values for the given day (excluding outliers) are represented by the lowest and highest lines, respectively. The box represents the 2nd and 3rd quartiles of the data, with the middle line representing the median of the data. Any outliers are represented by circles above or below the minimum and maximum value lines.

Figure 13: Fire-induced 500 hPa geopotential height perturbations and wind field over Domain 2 of the Creek Fire on 5 September 2020 23:30:00 UTC. Blue arrows indicate wind vectors from the No Fire run and red arrows indicate wind vectors from the Fire Run.

Figure 14: Maximum fire-induced surface geopotential height perturbations for a) surface, b) 600 hPa, and c) 500 hPa pressure levels over the regions of positive fire heat flux. The maximum spike on panel c) is outside of the plot scale and reaches 17.7 m.

Figure 15: 10-meter Horizontal Convergence of the Creek Fire on 5 September 2020 22:45:00 UTC.

Figure 16: Radar analysis for the Creek Fire on 8 September 2020 UTC where a) is Reflectivity and b) is Correlation Coefficient

Figure 17: a) Accumulated Precipitation for the Fire run of the Creek Fire over the full ten-day period. b) Fire-Induced Accumulated Precipitation for the Creek Fire for the full ten-day period.

Figure 18: Overall dead fuel moisture content for vegetation of the Creek Fire on 12 September 2020 12:00:00 UTC.

Figure 1.

Thomas Fire Domain Configuration

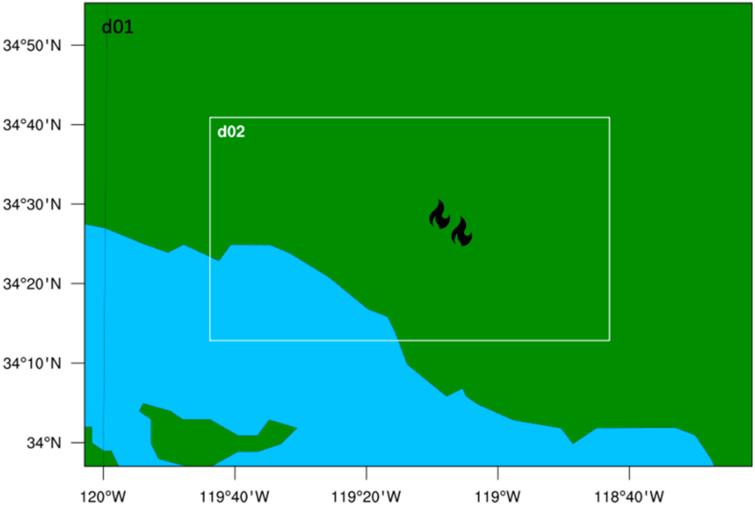

Figure 2.

Creek Fire Domain Configuration

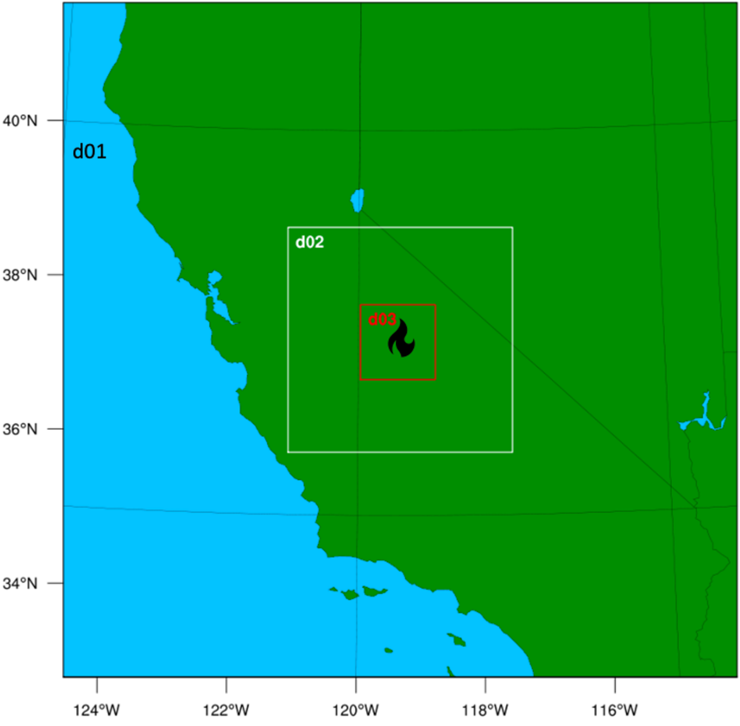

Figure 3.

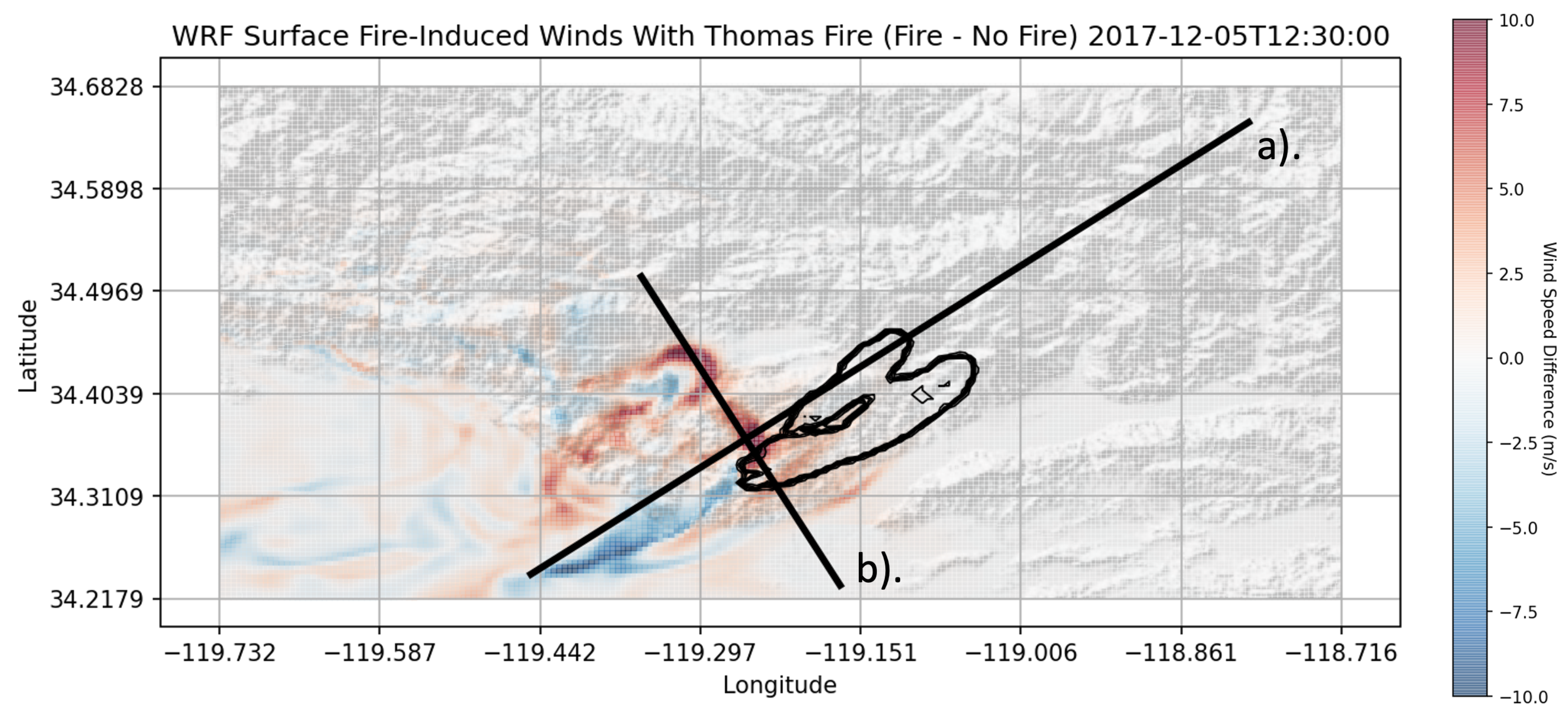
WRF Surface Fire-Induced Winds With Thomas Fire (Fire - No Fire) 2017-12-05T12:30:00
Latitude
34.6828
34.5898
34.4969
34.4039
34.3109
34.2179
Longitude
−119.732
−119.587
−119.442
−119.297
−119.151
−119.006
−118.861
−118.716
a).
b).
Wind Speed Difference (m/s)
10.0
7.5
5.0
2.5
0.0
−2.5
−5.0
−7.5
−10.0

Figure 4.

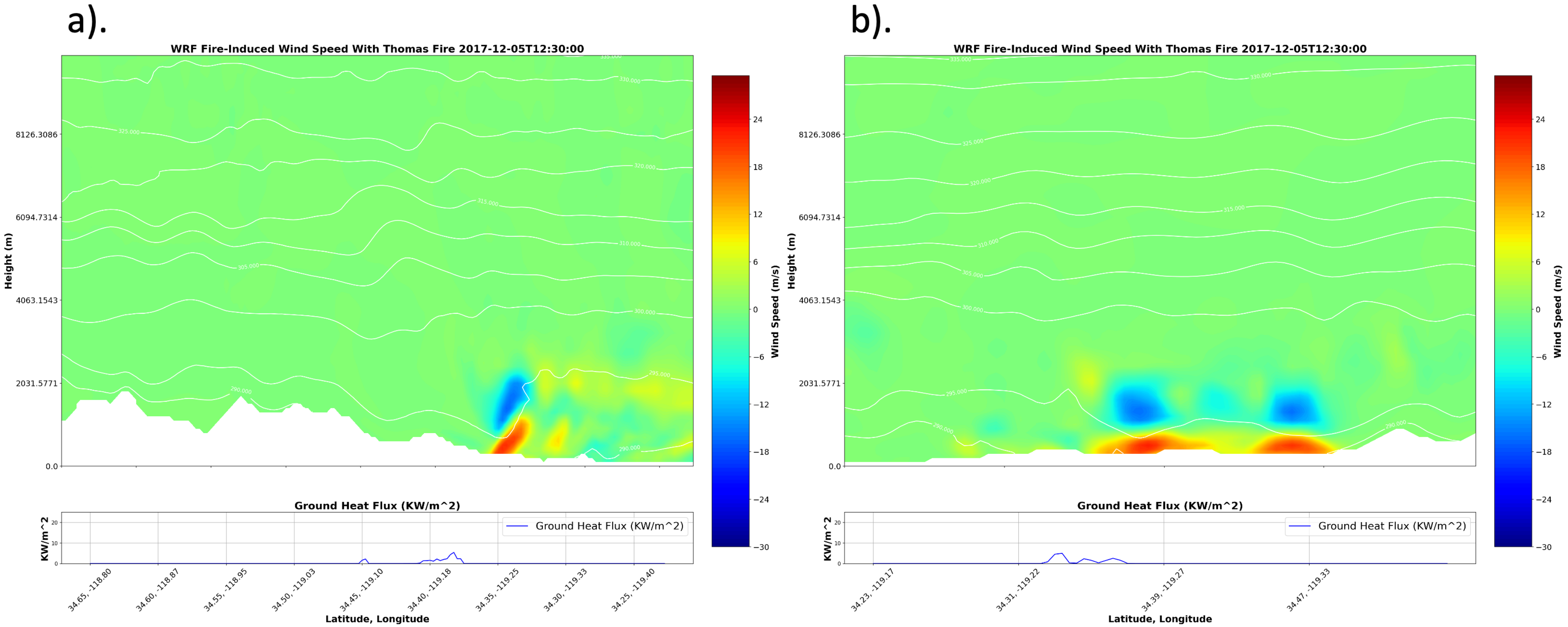

a).
WRF Fire-Induced Wind Speed With Thomas Fire 2017-12-05T12:30:00
Height (m)
8126.3086
6094.7314
4063.1543
2031.5771
0.0
Wind Speed (m/s)
24
18
12
6
0
−6
−12
−18
−24
−30
Ground Heat Flux (KW/m^2)
KW/m^2
Ground Heat Flux (KW/m^2)
34.65, -118.80
34.60, -118.87
34.55, -118.95
34.50, -119.03
34.45, -119.10
34.40, -119.18
34.35, -119.25
34.30, -119.33
34.25, -119.40
Latitude, Longitude
b).
WRF Fire-Induced Wind Speed With Thomas Fire 2017-12-05T12:30:00
Height (m)
Wind Speed (m/s)
Ground Heat Flux (KW/m^2)
KW/m^2
Ground Heat Flux (KW/m^2)
34.23, -119.17
34.31, -119.22
34.39, -119.27
34.47, -119.33
Latitude, Longitude

Figure 5.

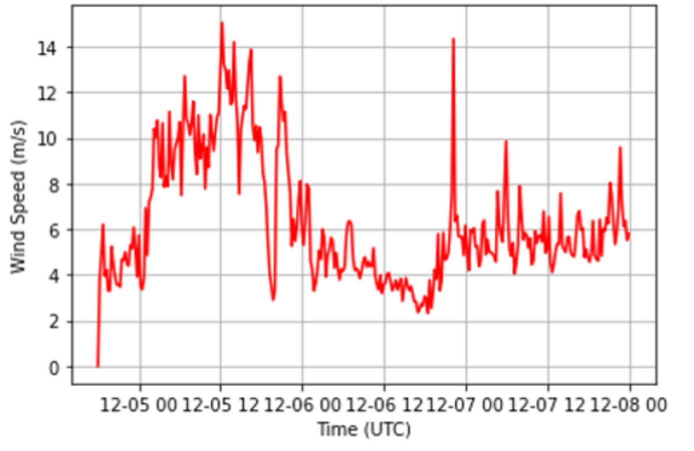

14
12
10
8
6
4
2
0
Wind Speed (m/s)
12-05 00
12-05 12
12-06 00
12-06 12
12-07 00
12-07 12
12-08 00
Time (UTC)

Figure 6.

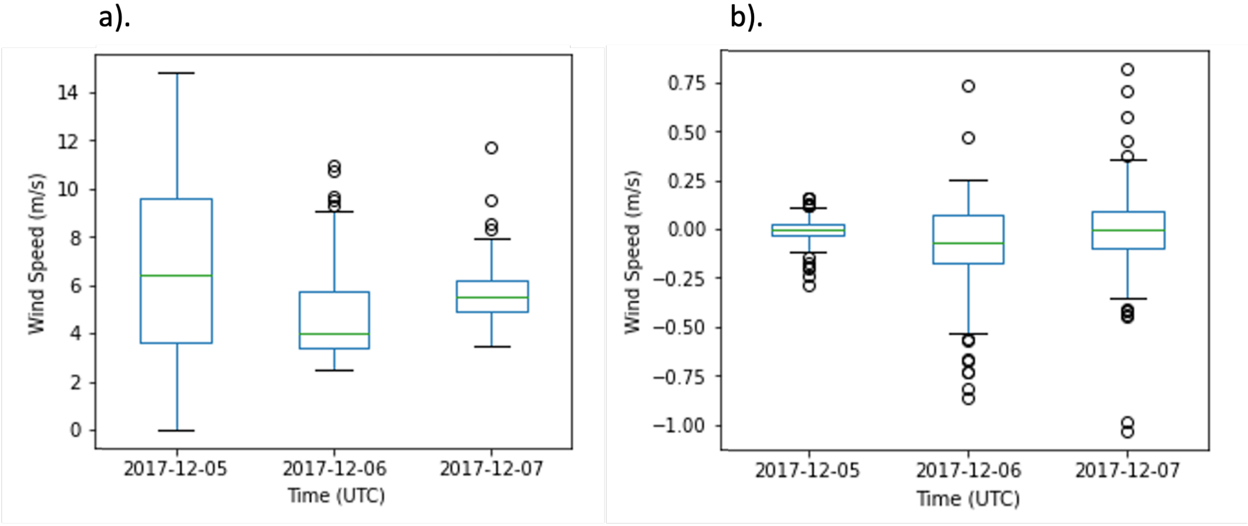
a).
b).
Wind Speed (m/s)
0
2
4
6
8
10
12
14
2017-12-05
2017-12-06
2017-12-07
Time (UTC)
Wind Speed (m/s)
−1.00
−0.75
−0.50
−0.25
0.00
0.25
0.50
0.75
2017-12-05
2017-12-06
2017-12-07
Time (UTC)

Figure 7.

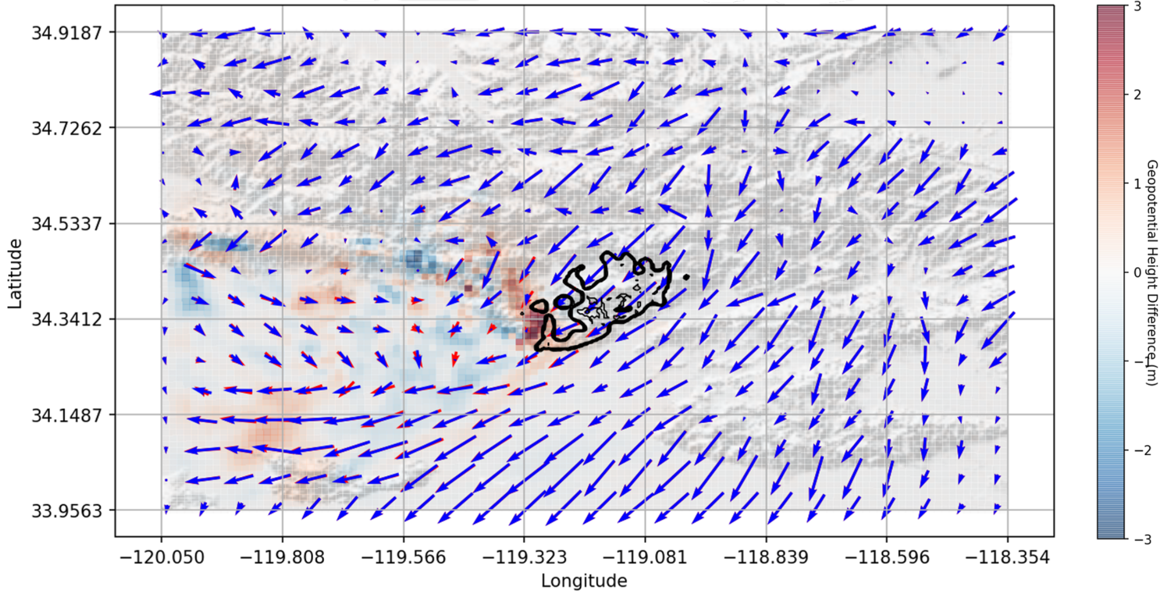
34.9187
34.7262
34.5337
34.3412
34.1487
33.9563
Latitude
−120.050
−119.808
−119.566
−119.323
−119.081
−118.839
−118.596
−118.354
Longitude
3
2
1
0
−1
−2
−3
Geopotential Height Difference (m)

Figure 8.

a).

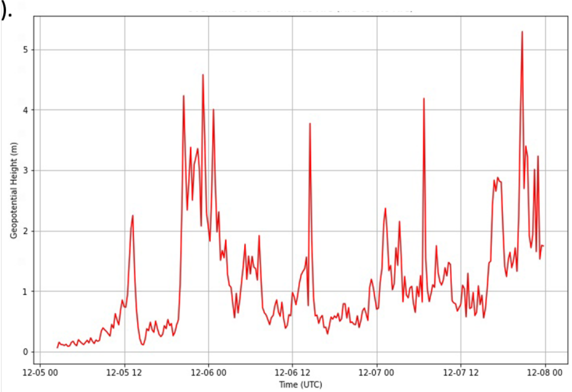
Geopotential Height (m)
0
1
2
3
4
5
12-05 00
12-05 12
12-06 00
12-06 12
12-07 00
12-07 12
12-08 00
Time (UTC)

b).

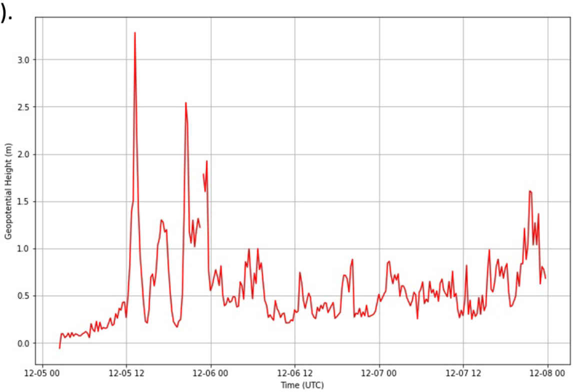
Geopotential Height (m)
0.0
0.5
1.0
1.5
2.0
2.5
3.0
12-05 00
12-05 12
12-06 00
12-06 12
12-07 00
12-07 12
12-08 00
Time (UTC)

c).

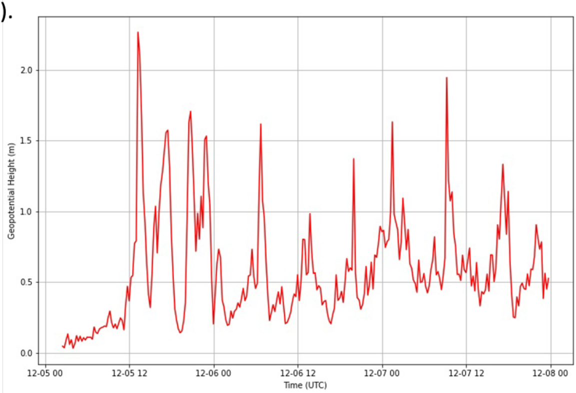
Geopotential Height (m)
0.0
0.5
1.0
1.5
2.0
12-05 00
12-05 12
12-06 00
12-06 12
12-07 00
12-07 12
12-08 00
Time (UTC)

Figure 9.

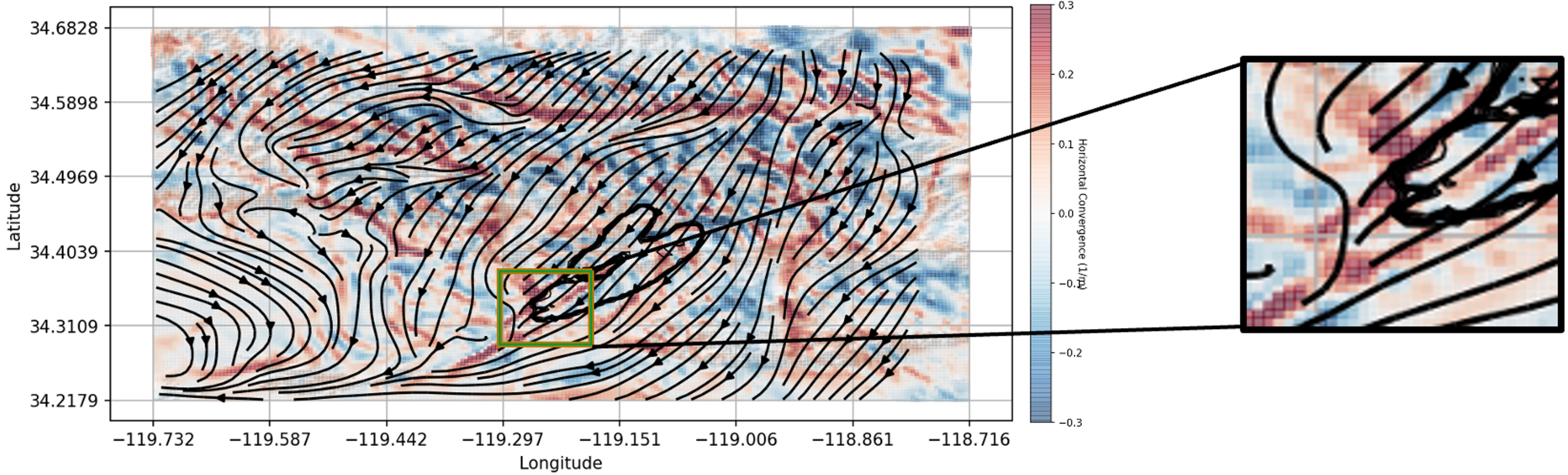
34.6828
34.5898
34.4969
34.4039
34.3109
34.2179
Latitude
−119.732
−119.587
−119.442
−119.297
−119.151
−119.006
−118.861
−118.716
Longitude
0.3
0.2
0.1
0.0
−0.1
−0.2
−0.3
Horizontal Convergence (1/m)

Figure 10.

a).

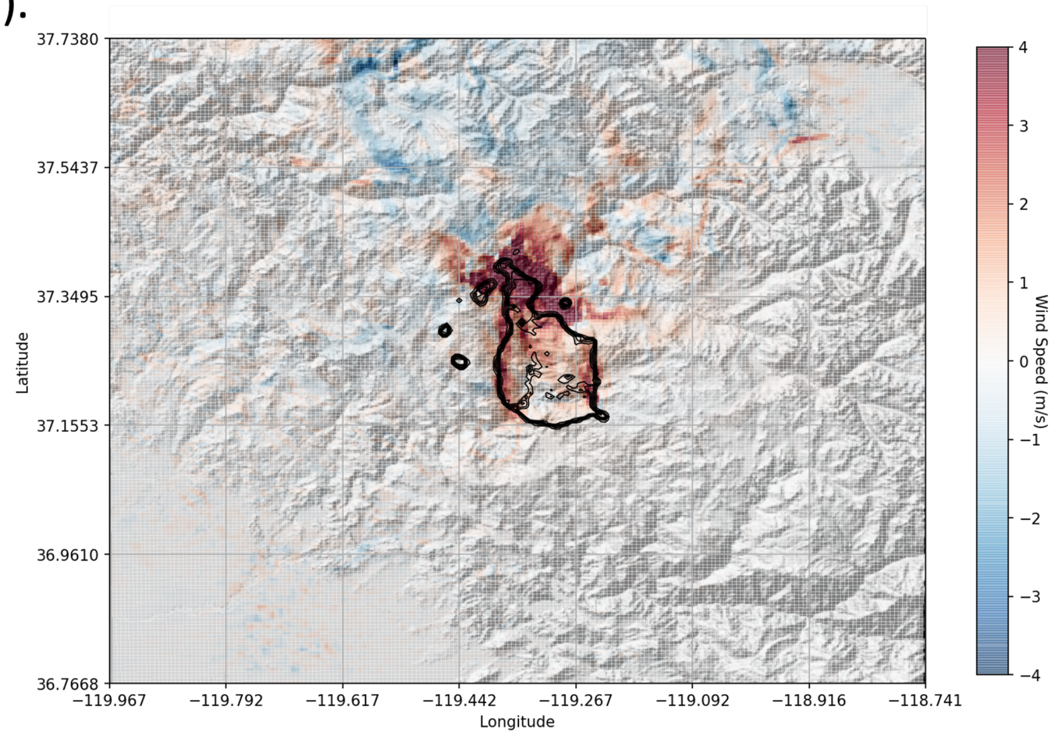

37.7380
37.5437
37.3495
37.1553
36.9610
36.7668
Latitude
−119.967
−119.792
−119.617
−119.442
−119.267
−119.092
−118.916
−118.741
Longitude
4
3
2
1
0
−1
−2
−3
−4
Wind Speed (m/s)

b).

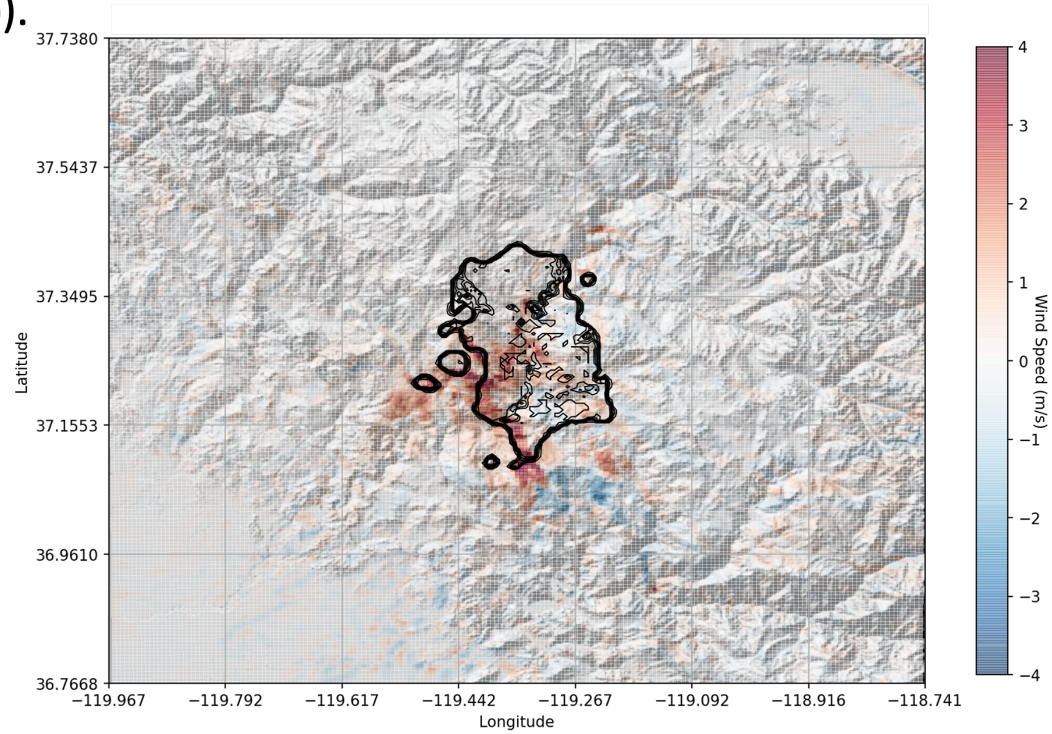

37.7380
37.5437
37.3495
37.1553
36.9610
36.7668
Latitude
−119.967
−119.792
−119.617
−119.442
−119.267
−119.092
−118.916
−118.741
Longitude
4
3
2
1
0
−1
−2
−3
−4
Wind Speed (m/s)

Figure 11.

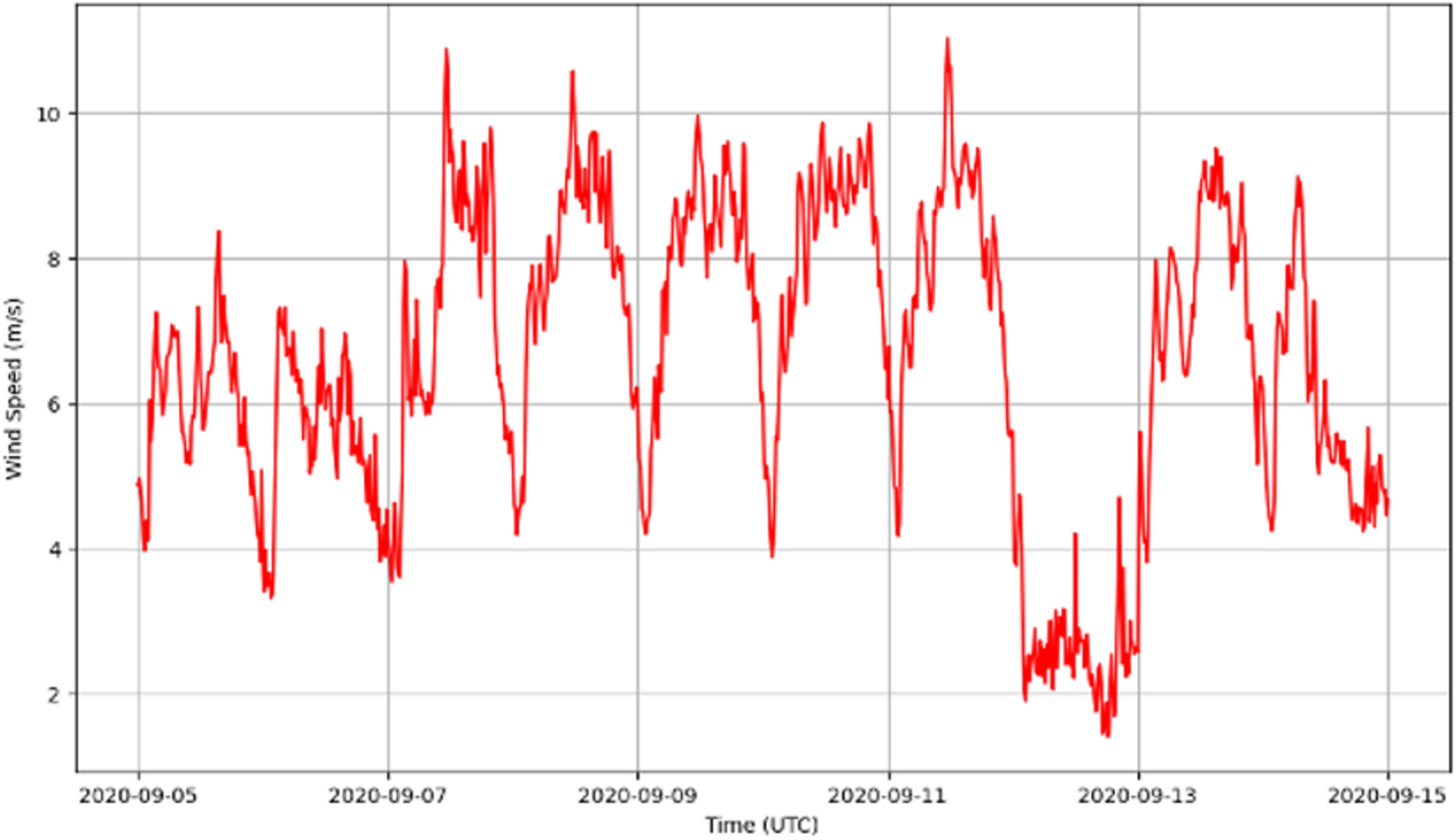

Wind Speed (m/s)
10
8
6
4
2
2020-09-05
2020-09-07
2020-09-09
2020-09-11
2020-09-13
2020-09-15
Time (UTC)

Figure 12.

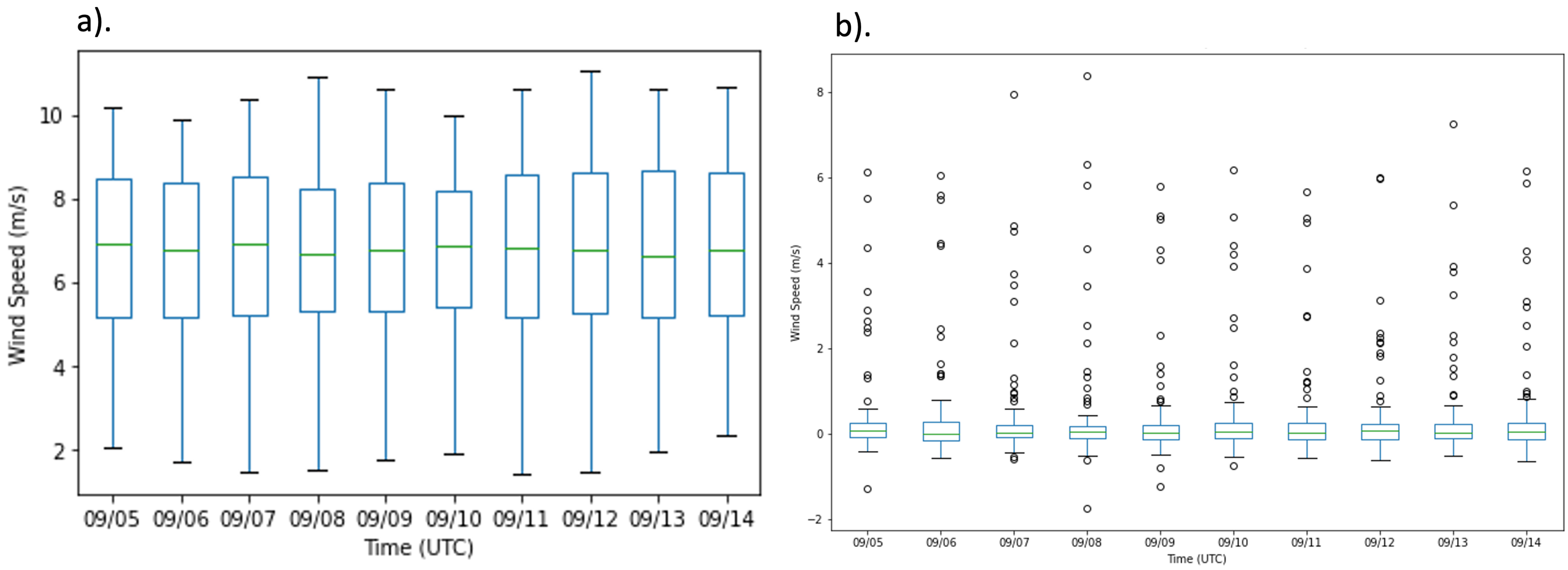
a).
Wind Speed (m/s)
10
8
6
4
2
09/05
09/06
09/07
09/08
09/09
09/10
09/11
09/12
09/13
09/14
Time (UTC)
b).
Wind Speed (m/s)
8
6
4
2
0
−2
09/05
09/06
09/07
09/08
09/09
09/10
09/11
09/12
09/13
09/14
Time (UTC)

Figure 13.

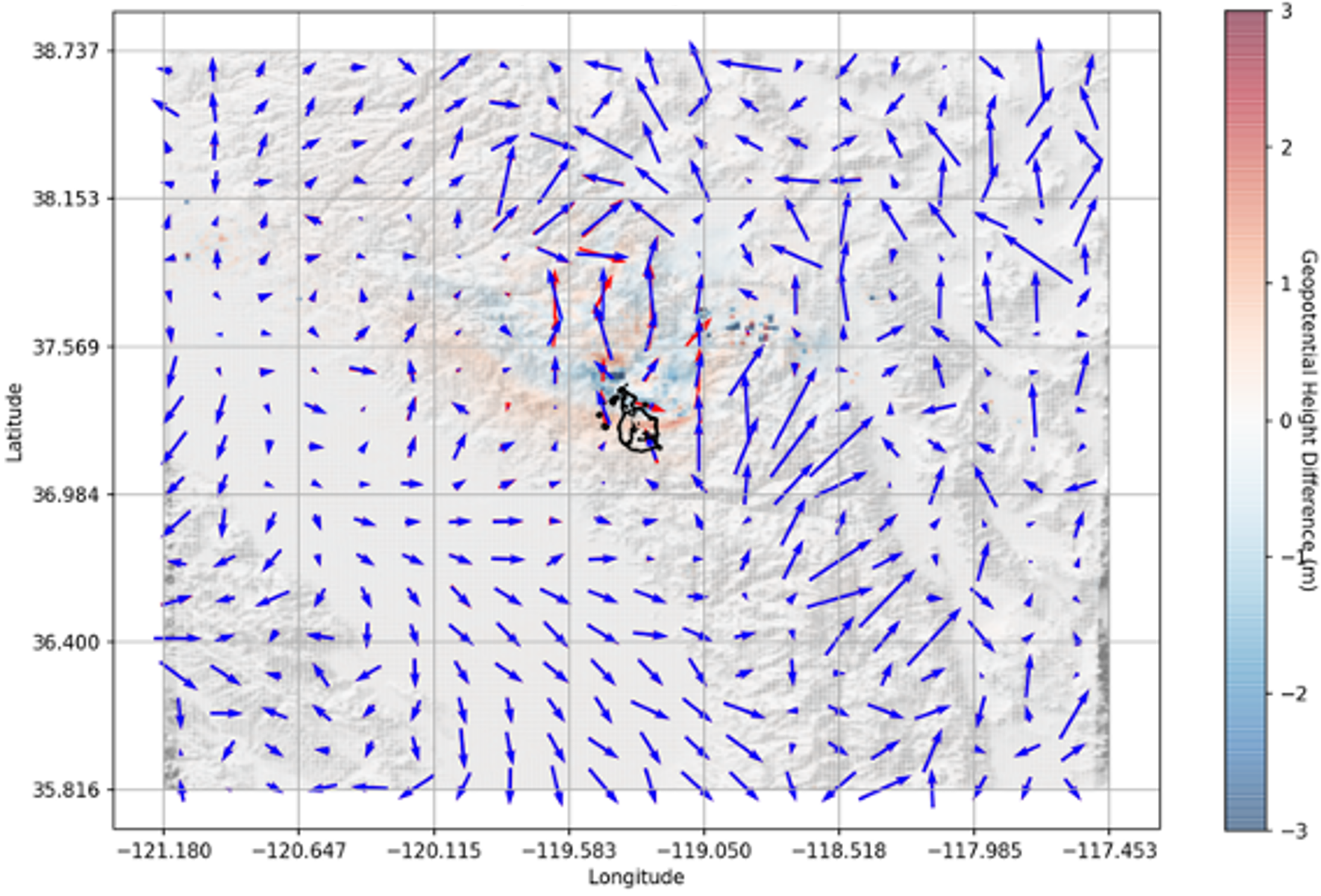

38.737
38.153
37.569
36.984
36.400
35.816
Latitude
−121.180
−120.647
−120.115
−119.583
−119.050
−118.518
−117.985
−117.453
Longitude
3
2
1
0
−1
−2
−3
Geopotential Height Difference (m)

Figure 14.

a).

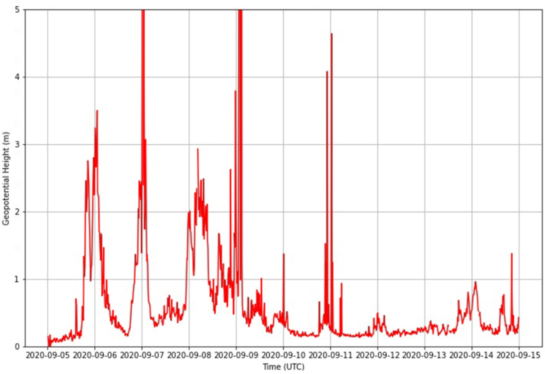

0
1
2
3
4
5
Geopotential Height (m)
2020-09-05 2020-09-06 2020-09-07 2020-09-08 2020-09-09 2020-09-10 2020-09-11 2020-09-12 2020-09-13 2020-09-14 2020-09-15
Time (UTC)

b).

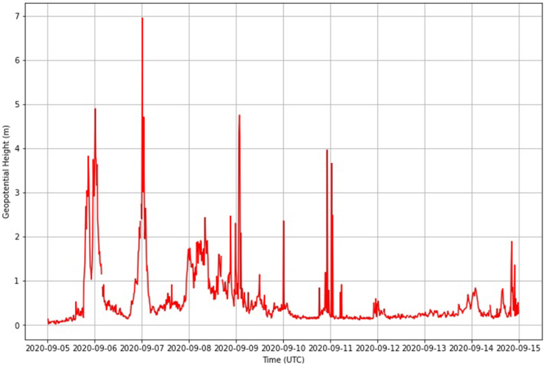

0
1
2
3
4
5
6
7
Geopotential Height (m)
2020-09-05 2020-09-06 2020-09-07 2020-09-08 2020-09-09 2020-09-10 2020-09-11 2020-09-12 2020-09-13 2020-09-14 2020-09-15
Time (UTC)

c).

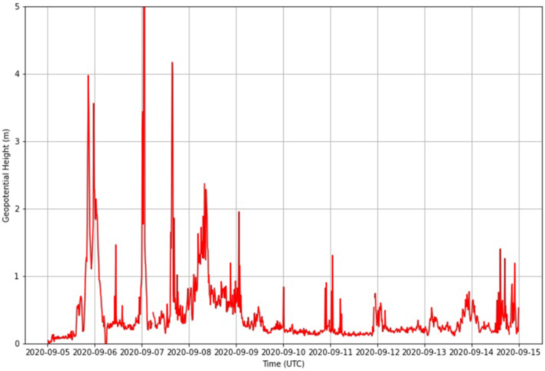

0
1
2
3
4
5
Geopotential Height (m)
2020-09-05 2020-09-06 2020-09-07 2020-09-08 2020-09-09 2020-09-10 2020-09-11 2020-09-12 2020-09-13 2020-09-14 2020-09-15
Time (UTC)

Figure 15.

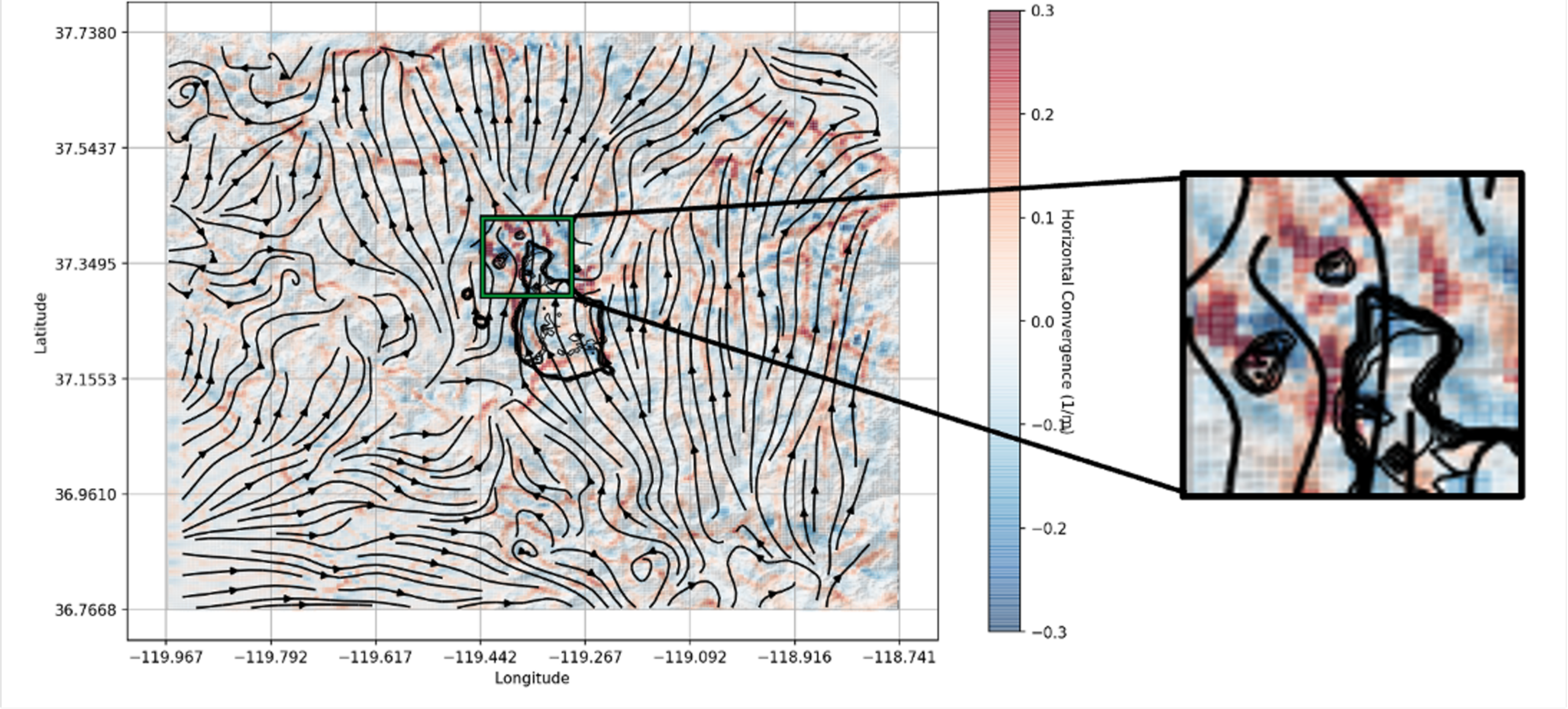

37.7380
37.5437
37.3495
37.1553
36.9610
36.7668
Latitude
−119.967
−119.792
−119.617
−119.442
−119.267
−119.092
−118.916
−118.741
Longitude
0.3
0.2
0.1
0.0
−0.2
−0.3
Horizontal Convergence (1/m)

Figure 16.

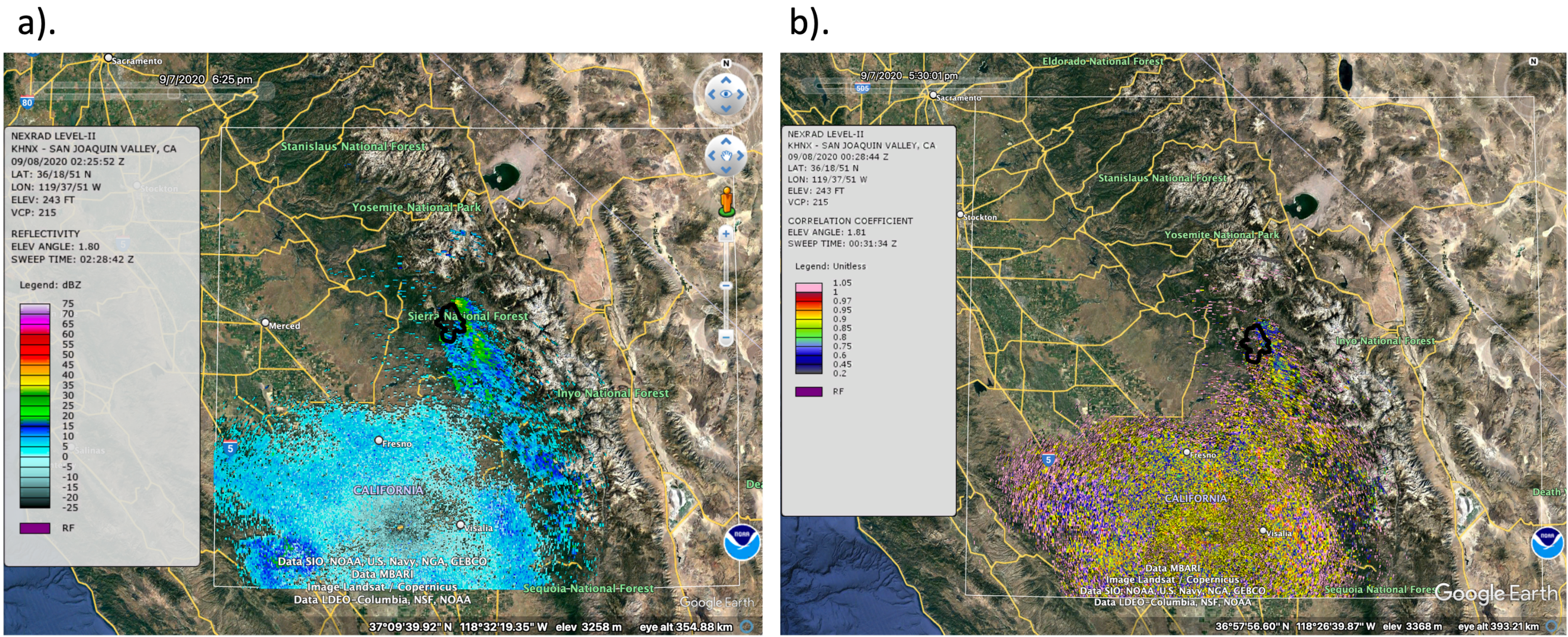
a).
b).
NEXRAD LEVEL-II
KHNX - SAN JOAQUIN VALLEY, CA
09/08/2020 02:25:52 Z
LAT: 36/18/51 N
LON: 119/37/51 W
ELEV: 243 FT
VCP: 215
REFLECTIVITY
ELEV ANGLE: 1.80
SWEEP TIME: 02:28:42 Z
Legend: dBZ
RF
9/7/2020 6:25 pm
37°09'39.92" N 118°32'19.35" W elev 3258 m eye alt 354.88 km
NEXRAD LEVEL-II
KHNX - SAN JOAQUIN VALLEY, CA
09/08/2020 00:28:44 Z
LAT: 36/18/51 N
LON: 119/37/51 W
ELEV: 243 FT
VCP: 215
CORRELATION COEFFICIENT
ELEV ANGLE: 1.81
SWEEP TIME: 00:31:34 Z
Legend: Unitless
RF
9/7/2020 5:30:01 pm
36°57'56.60" N 118°26'39.87" W elev 3368 m eye alt 393.21 km

Figure 17.

a).

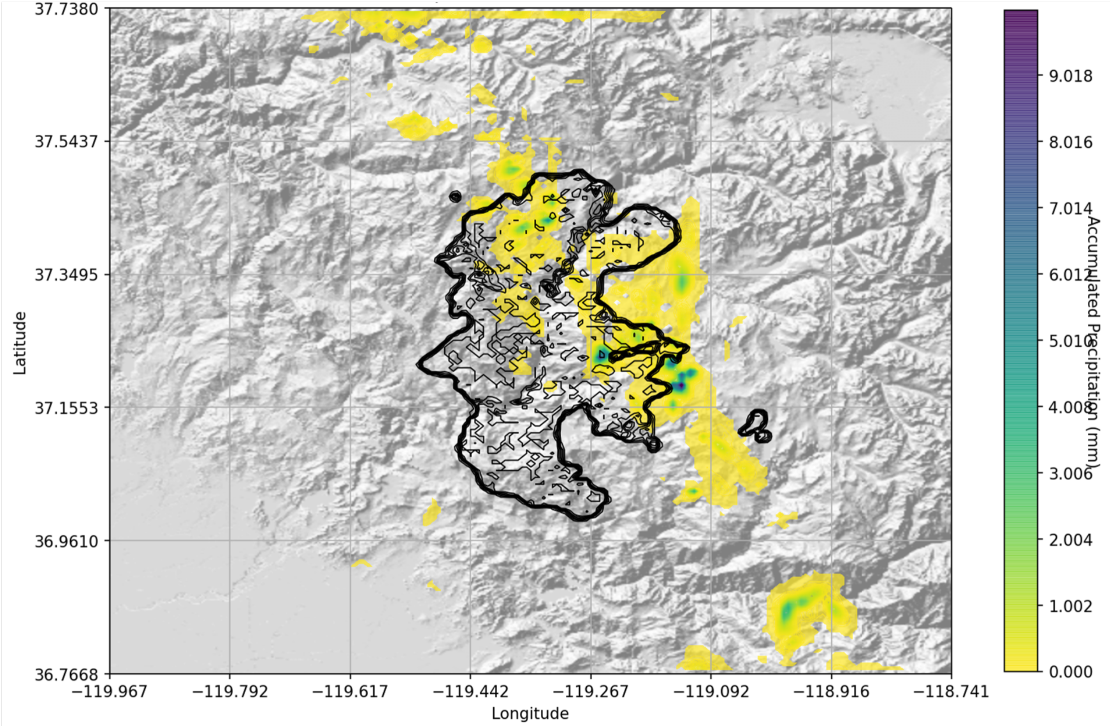
37.7380
37.5437
37.3495
37.1553
36.9610
36.7668
Latitude
−119.967
−119.792
−119.617
−119.442
−119.267
−119.092
−118.916
−118.741
Longitude
9.018
8.016
7.014
6.012
5.010
4.008
3.006
2.004
1.002
0.000
Accumulated Precipitation (mm)

b).

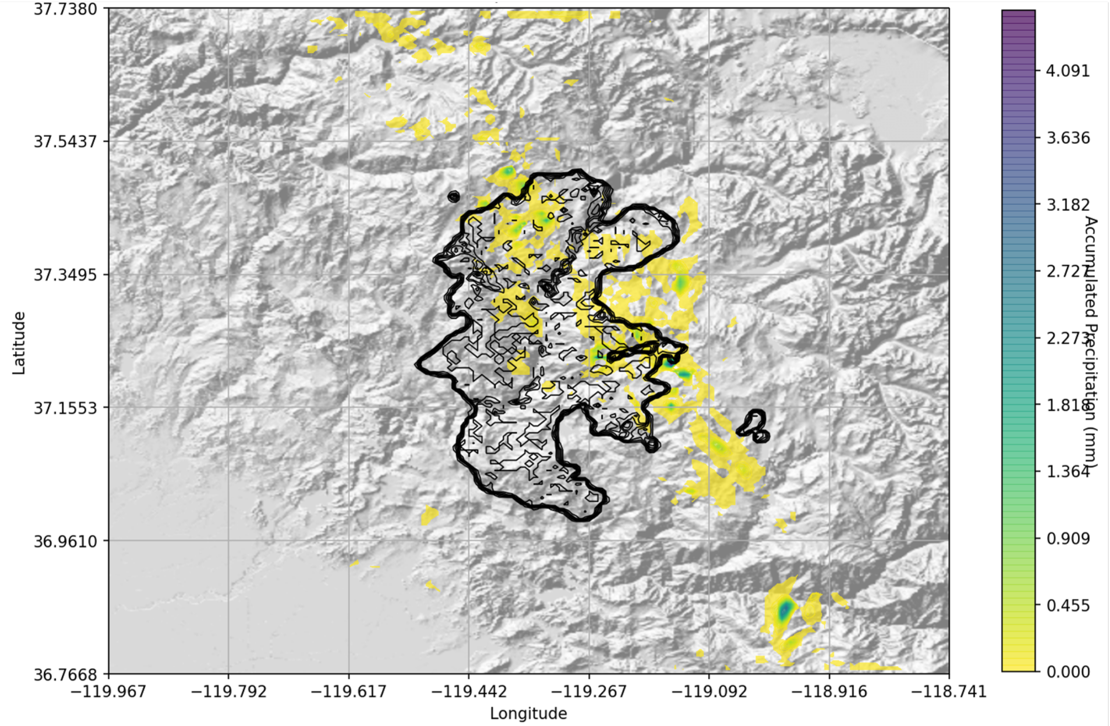
37.7380
37.5437
37.3495
37.1553
36.9610
36.7668
Latitude
−119.967
−119.792
−119.617
−119.442
−119.267
−119.092
−118.916
−118.741
Longitude
4.091
3.636
3.182
2.727
2.273
1.818
1.364
0.909
0.455
0.000
Accumulated Precipitation (mm)

Figure 18.

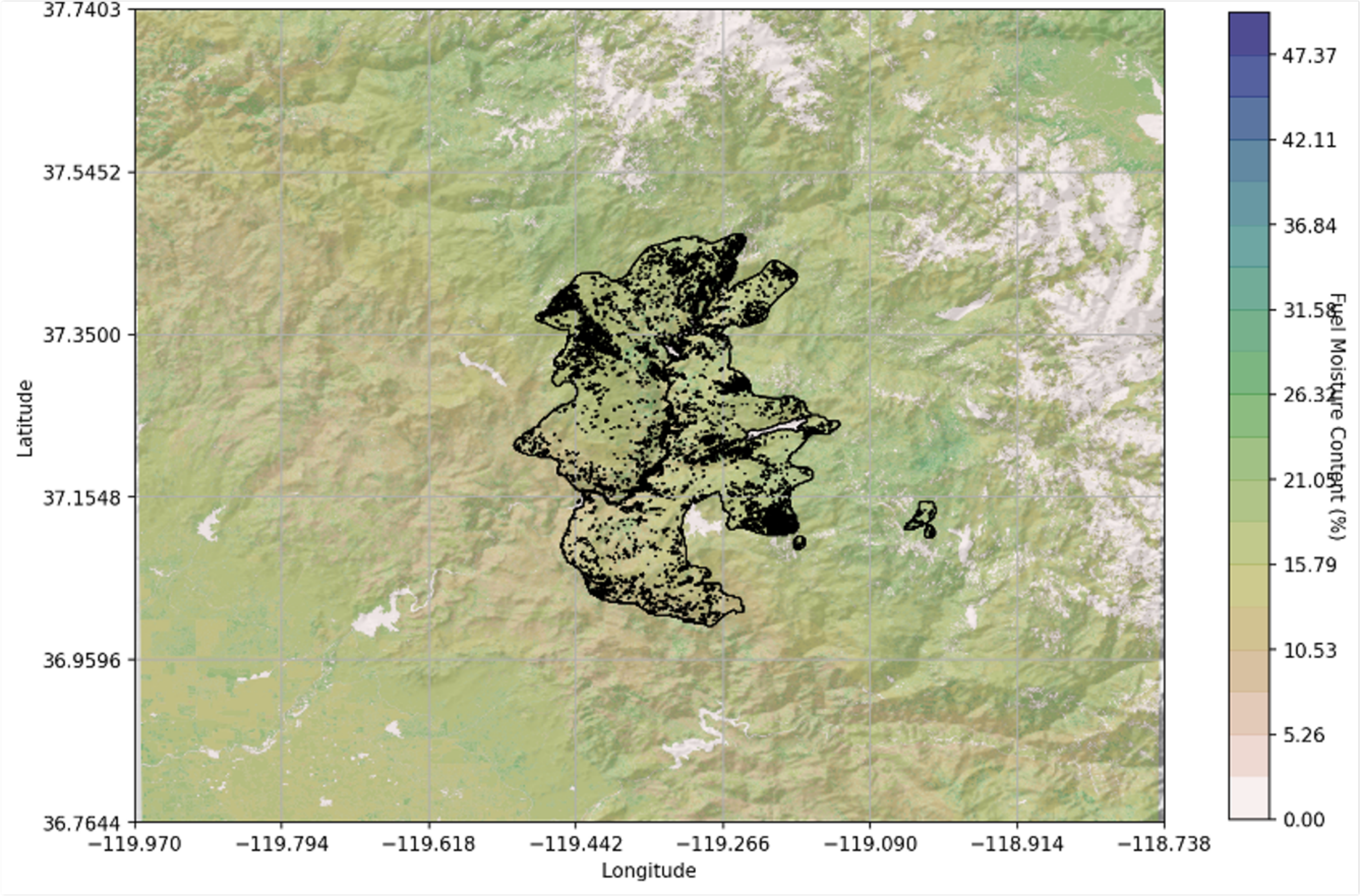

37.7403
37.5452
37.3500
37.1548
36.9596
36.7644
Latitude
−119.970
−119.794
−119.618
−119.442
−119.266
−119.090
−118.914
−118.738
Longitude
47.37
42.11
36.84
31.58
26.32
21.05
15.79
10.53
5.26
0.00
Fuel Moisture Content (%)